# Stability under electron irradiation of some layered hydrated minerals

Marie-Noëlle de Noirfontaine, Mireille Courtial, A. Alessi, S. Tusseau-Nenez, E. Garcia-Caurel, O. Cavani, Céline Cau Dit Coumes, Dominique Gorse–pomonti

# Stability under electron irradiation of some layered hydrated minerals

M.-N. de Noirfontaine[a,*], M. Courtial[a], A. Alessi[a], S. Tusseau-Nenez[b], E. Garcia Caurel[c], O. Cavani[a], C. Cau dit Coumes[d], D. Gorse-Pomonti[a]

[a] Laboratoire des Solides Irradiés, CEA-DRF-IRAMIS, CNRS, Ecole polytechnique, Institut Polytechnique de Paris, 91120, Palaiseau, France
[b] Laboratoire de Physique de la Matière Condensée, CNRS, Ecole polytechnique, Institut Polytechnique de Paris, 91120, Palaiseau, France
[c] Laboratoire de Physique des Interfaces et des Couches Minces, CNRS, Ecole polytechnique, Institut Polytechnique de Paris, F-91128 Palaiseau Cedex, France
[d] CEA, DES, ISEC, DPME, SEME, Univ Montpellier, Marcoule, France

Corresponding author: marie-noelle.de-noirfontaine@polytechnique.edu (M.-N. de Noirfontaine)

Keywords: portlandite, brucite, gypsum, brushite, structural damage, phase transformation

## Abstract

The structural damages caused to some layered hydrated minerals by 2.5 MeV electron irradiation using the SIRIUS platform were studied by powder X-Ray diffraction and, in some cases, by $^{1}$H MAS-NMR spectroscopy. It is clearly demonstrated that the radiation damages are distinguishable from the heating effects. It is shown that: i) in all cases electron irradiation leads to distortions of the unit cell and very limited volume expansion, compared to heating; ii) radiation damages increase with increasing the structural complexity of the mineral; iii) portlandite $Ca(OH)_2$ and brucite $Mg(OH)_2$ remain crystalline up to high doses (a few GGy), with appearance of stacking fault disorder especially in brucite; iv) brushite $CaHPO_4.2H_2O$ and gypsum $CaSO_4.2H_2O$ undergo a phase transformation of type amorphization for brushite involving the strongest intralayer H bond between the acidic proton and the phosphate tetrahedral, and decomposition for gypsum involving interlayer H bonds between water molecules.

## 1. Introduction

The technological context of the study is the optimization of cement-based materials for nuclear applications, such as cemented waste packages [1, 2] or structural concrete exposed to irradiation [3]. These cementitious matrices are composed of hydrated minerals, some of which are lamellar (portlandite $Ca(OH)_2$, brucite $Mg(OH)_2$, brushite $CaHPO_4.2H_2O$, gibbsite $Al(OH)_3$...). Such compounds are also of interest for geological purposes (as constituent or model materials of the earth's crust and mantle [4, 5] or Mars crust [6]), for construction (as raw materials, compounds or additives for cements or plasters [7]), or even for biomedical research (as bone and dental substitute materials [8, 9]). While data exists on the structural damage of these minerals as a function of a number of physico-chemical parameters (temperature, pressure, atmosphere, pH, etc.), information about the influence of irradiation, and more specifically of electron irradiation, on their crystal structure at high integrated dose is still very limited.

Until very recently, there has been practically no research on energetic electron radiation damages to hydroxides or oxy-hydroxides, at low flux ($10^{13}$ - $10^{14}$ $e^{-}.cm^{-2}.s^{-1}$), compared to the ones generated in transmission electron microscopes (TEM) at $10^{17}$ - $10^{23}$ $e^{-}.cm^{-2}.s^{-1}$. Only oxides of interest

for nuclear applications such as oxide fuels and oxide matrices for radioactive waste immobilization [10-13] or semiconductor oxides for next generation photovoltaic devices have been the subject of some research effort essentially [14, 15]. To these materials, we can also add some simple binary refractory oxides which have been studied for fundamental reasons since MeV electron irradiation has the specificity to form only point defects and no cascades in materials. Thus, it is possible to measure directly the threshold displacement energy of the anionic or cationic components of the refractory oxides, and to study their defect production mechanisms in relation with their microstructural properties (segregation, phase transformation, gas bubbles formation…) [16, 17].

In situ transmission electron microscopy during irradiation by energetic electrons (200-400 keV typically) and ions has shown that all the studied materials (zeolites, clays, (hydroxy)apatites..) are susceptible to irradiation-induced amorphization [18]. Wang et al. also mention that even partial amorphization can cause a drastic reduction (up to 95%) in ion-exchange and sorption/desorption capacities of zeolite for radionuclides, such as Cs and Sr. This may be beneficial for radioactive waste management since the release of sorbed or ion-exchanged radionuclides is then mitigated [18].

However, studies devoted to the influence of electrons on inorganic crystalline materials that contain water of hydration are very scarce. As yet, there is very few data in literature on electron radiation damage effects on layered hydroxides for high doses, up to several GGy (dose rate around $10^8$ Gy/h), apart from the clay minerals studied in the context of radioactive waste disposal [19, 20]. Even for smaller doses reached under gamma irradiation, studies devoted to the structural stability of these compounds are also rather scarce. For doses between 10 kGy and 100 MGy, the stability of brucite under gamma irradiation (dose rate around $5x10^4$ Gy/h) was investigated by Shpak et al. [21], showing the dehydration of brucite. Baral et al. [22] evidenced a decrease in the basal spacing of calcium silicate hydrates (C-S-H) due to interlayer water removal and a slight depolymerization of their silicate structure. In parallel with a study of some cement-based materials envisaged for radwaste treatment and conditioning, we recently investigated the resistance to electron irradiation of some of their constitutive hydrates, starting with the apparently more simple structures (gibbsite $Al(OH)_3$ and katoite $Ca_3Al_2(OH)_{12}$ for calcium aluminate cements, as well as portlandite $Ca(OH)_2$ for calcium silicate cement (leaving aside ettringite, monosulfate and C-S-H, the calcium silicate hydrate), which was compared to isostructural brucite $Mg(OH)_2$ [23, 24]. We then continued with brushite $CaHPO_4.2H_2O$, precipitating in certain types of calcium phosphate cements [25].

We were impressed by the remarkable stability of both portlandite and brucite powders after electron irradiation at high doses (a few GGy) [23], which largely exceeded the typical doses integrated by cemented waste packages over their lifetime (a few MGy). This contrasts with the results obtained under high pressure on deuterated compounds, showing that brucite remains crystalline under pressure up to 50 GPa, even up to 78 GPa at high temperature [26] whereas portlandite amorphizes above 10 GPa, reversibly around 12 GPa [27]. In a parent paper [28], we have seen that, by comparison with portlandite and brucite, and also gibbsite [24], brushite converts directly to calcium pyrophosphate under electron irradiation. Interestingly, the behavior of brushite under electron irradiation differs from its evolution upon heating, which first leads to its progressive transformation into monetite $CaHPO_4$ and an amorphous phase, and then to calcium pyrophosphates $Ca_2P_2O_7.xH_2O$ under more severe heating conditions (see § 2.4.2). The fact that brushite amorphizes under electron irradiation is not the key result since it is well known that amorphization of ceramic-like materials may occur with all types of radiation, whatever (light or heavy) ions, neutrons and electrons alike provided that the sample

temperature remains below a critical value [29]. The important point is that brushite amorphizes at low electron flux, three orders of magnitude lower than in a TEM.

In this paper, the focus is placed on four layered hydrated minerals with increasing structural complexity, going from simple sheets of $M(OH)_6$ octahedra in brucite and portlandite, to the complex sheets made of $CaO_8$ polyhedra and sulphate or phosphate tetrahedra in gypsum and brushite respectively. The objective is to compare their structural evolution due to energetic (2.5 MeV) electron irradiation at much lower flux than the ones typically reached in a transmission electron microscope, by using the PELLETRON NEC accelerator of the SIRIUS platform available at the LSI laboratory. Powder X-Ray Diffraction is here the main technique employed to estimate the damages caused by irradiation. One could quite rightly argue that it is not, by far, the more appropriate method in order to analyze in-depth the damages since hydrogen is a weak scatterer of X-rays. But precisely, since this is the first comparative study of radiation damages to isostructural brucite and portlandite on one side, and to topologically identical gypsum and brushite on the other side, this not-particularly-sensitive technique not only proves to be a powerful tool to classify the compounds regarding their resistance to irradiation, but also permits to identify the bonds affected by electron irradiation.

## 2. Experimental

### 2.1. Materials

One commercial powder of portlandite $Ca(OH)_2$ (Prolabo, 96 wt.% purity) and two commercial powders of brucite $Mg(OH)_2$ (Prolabo, 99.7 wt.% purity, and Sigma-Aldrich 99.8 wt.% purity) were used. For portlandite, the main impurities were determined by X-ray fluorescence: MgO: 0.838 wt.%, $SiO_2$: 0.406 wt.%, $Al_2O_3$: 0.084 wt.%, $Fe_2O_3$: 0.071 wt.%, $SO_3$: 0.048 wt.%, MnO: 0.022 wt.%, Cl: 0.005 wt.%, $TiO_2$: 0.001 wt.%. For the powders of brucite provided by Prolabo, the impurities determined by X-ray fluorescence were: $SiO_2$: 0.845 wt.%, $SO_3$: 0.068 wt.%, CaO: 0.061 wt.%, $Fe_2O_3$: 0.008 wt.%, $TiO_2$: 0.002 wt.%, $K_2O$: 0.001 wt.%, $P_2O_5$: 0.001 wt.%. For the powders of brucite provided by Sigma Aldrich, the main impurities determined by ICP were: Na (10.8 ppm), B (5.8 ppm), Ca (4.2 ppm), Mn (1.9 ppm), Fe (1.2 ppm), Sr < 0.1 ppm.

In ambient air, some unavoidable carbonation of the portlandite powders occurs according to the reaction $Ca(OH)_2 + CO_2 \rightarrow CaCO_3 + H_2O$. Consequently, the presence of a significant amount of calcite was found in their XRD patterns. Three different samples, containing initially about 1.5 wt.%, 4 wt.% and 15 wt.% of calcite $CaCO_3$, were irradiated. They will be referred to as P1.5, P4 and P15 in the following. The sample of brucite provided by Prolabo, referred here to as B-PRO, contained ~ 0.6 wt.% of periclase MgO. No periclase was detected in the brucite sample provided par Sigma-Aldrich, referred to as B-SA in the following.

A powder of gypsum $CaSO_4.2H_2O$ was obtained by manual grinding a natural single crystal. Its starting thermal decomposition was found around 110°C by thermogravimetry, in agreement with the literature (section 2.3.2). A commercial powder of brushite $CaHPO_4.2H_2O$ (purity > 98 wt.%, Acros Organics) was also used. The sample contained 95.80 wt.% brushite, 2.05 wt.% monetite $CaHPO_4$ and 2.15 wt.% newberyite $MgHPO_4.2H_2O$ [28].

The powders were pressed in order to make discs (13 mm in diameter (1.33 $cm^2$) and about 1 mm thick) for irradiation experiments. Two runs were conducted on B-SA brucite, referred to as B-SA(1) and B-SA(2) in the following.

### 2.2. Powder X-Ray diffraction

The pellets of virgin and irradiated samples were slightly ground manually in an agate mortar and then front-loaded into the sample holder. X-ray diffraction data were collected at room temperature, using two powder X-ray diffractometers in the Bragg Brentano geometry (θ/θ) configured with CuKα radiation. For portlandite with 1.5 and 15 wt.% calcite, XRD data were collected with a Panalytical X'Pert diffractometer with a X'Celerator detector, working at 45 kV and 40 mA [23]. For the other samples, the data were recorded on a high resolution Bruker D8 Advance diffractometer working at 40 kV and 40 mA, with a LynxEye XE-T detector [28]. For brushite, each scan was repeated three times to improve the signal-to-noise ratio. Moreover, to study the flux effects, the brushite powders were deposited on a Si zero-background sample holder.

Rietveld analysis was performed using the TOPAS Software (Bruker-AXS; V6, 2016) and ISCD database. For all adjustments, the refined parameters were the phase scale factors, sample displacement, background modeled by a Chebyshev polynomial combined with a 1/X term, unit cell and microstructural parameters. The atomic positions, site occupancies and temperature factors were kept constant during the refinement. Lamellar structures are sensitive to a preferential orientation of grains in the sample: this was corrected using the March-Dollase model [30]. The starting crystallographic parameters for portlandite, brucite, gypsum and brushite are listed in Table 1 [31-34]. For the decomposition products of gypsum, the starting structural models of bassanite and anhydrite (β-forms) were respectively those of Bezou et al. [35] (ICSD-69060, I2 monoclinic space group) and Cheng et al. [36] (ICSD-15876, Amma orthorhombic space group). The crystal structures used for the two minor phases of brushite, monetite $CaHPO_4$ and newberyite $MgHPO_4.3H_2O$, were based on the ICSD917 and ICSD8228 structural dataset.

### 2.3. $^1$H MAS-NMR spectroscopy

Solid-state NMR spectroscopy is a well-adapted method to characterize the atomic level structure in solids, regardless of their crystallinity. $^1$H proton, with its spin ½, its high abundance (99.98%) and high gyromagnetic ratio ($26.75\times107$ rad.$T^{-1}$.$s^{-1}$), is a nucleus of choice for NMR studies. However, in solids, anisotropic interactions give rise to a strong network of homonuclear dipolar couplings between protons, which are often difficult to average to zero at commonly accessible magic angle spinning rates. This results in a broadening of $^1$H spectral lines, and a narrow span of chemical shifts (≈15 ppm) [37].

Pristine and irradiated brushite were nevertheless characterized by $^1$H MAS-NMR spectroscopy with a Varian VNMRS 600 MHz spectrometer operating at a magnetic field $B_0$ of 14 T. The spectra were acquired at 599.81 MHz, using a 3.2 mm T3 MAS probe with $ZrO_2$ rotors spun at 20 kHz, a recycle delay of 30 s and 32 transients. Since the stator of the probe contained Vespel, a hydrogenated polymer, the DEPTH sequence, composed of one π/2 initial excitation pulse (pulse duration = 2.5 µs), and two consecutive π pulses (pulse duration = 5 µs), was applied to suppress the probe background signal [38]. Note that the analysis of the corrected spectra could only be qualitative. Chemical shifts were referenced to external adamantane ($C_{10}H_{16}$) at 1.8 ppm.

### 2.4. Crystal structures

### 2.4.1 Portlandite and brucite: trigonal hydroxides

Portlandite $Ca(OH)_2$ and its isostructural brucite $Mg(OH)_2$ belong to the family of lamellar hydroxides. They are considered as simple models of hydrogen - bearing layered materials. Their crystal structure is composed of layers of distorted edge-sharing $[M(OH)_6]$ octahedra, with M = Ca, Mg (Mg being smaller than Ca), stacked along the **c**-axis. Each OH group is linked to three M atoms of its layer and surrounded by three oppositely oriented OH groups of the adjacent layer (Fig. 1). Portlandite and brucite being easy to cleave, as early as 1957, it was inferred that the interlayer interactions were weak, of the Van der Waals type [40]. For years however, the possible existence of hydrogen bonds between two adjacent layers was a matter of debate [27, 41]. It is now admitted that there are no H-bonds at room pressure, but only at high pressure [32]. An unusual and anisotropic thermal motion of the H atoms, essentially in the **ab** plane, has been reported very early by Busing and Levy [31, 40, 42, 43].

In the first single crystal neutron diffraction studies of portlandite, hydrogen is considered as occupying a single-site: this is the so-called "one-site model" [31], in which the atomic coordinates ($z_O$ and $z_H$) and anisotropic thermal parameters are refined. Later, the three-site split-atom model in which each H atom is disordered over three positions about the three-fold rotation, with equal occupancy (1/3) [42] was finally adopted. The one-site model, instead of the three - site model, is used here for convenience for both compounds.

Under heating, portlandite is more stable than brucite: portlandite decomposes into lime (CaO) and water vapor at ~ 723K (450°C) [44], whereas brucite starts to decompose into periclase (MgO) and water vapor [45] at ~ 583K (320°C).

### 2.4.2 Gypsum and brushite: monoclinic layered minerals

The crystal structure of gypsum $CaSO_4.2H_2O$ [33, 46] is composed of calcium sulfate $CaSO_4$ layers stacked along the **b** axis, linked (held) together by a layer of water molecules via "weak" hydrogen bonds (O1---H2-O3) along the **b** axis (Fig. 1, Table 2). Precisely, they consist of ziz-zag chains of $CaO_8$ polyhedra linked to zig–zag chains of $SO_4^{2-}$ tetrahedra, along the **a** axis. Six oxygens of the $CaO_8$ polyhedra are shared with the $SO_4$ tetrahedra and the remaining two oxygens are shared with water molecules. The water molecules that fill the interlayer space are identical in gypsum. Inside the layers, one notes the presence of a hydrogen bond (O1---H1-O3) oriented essentially along the **a** axis, described as "stronger" than the interlayer hydrogen bond (O1---H2-O3) [47] (Fig. 1, Table 2).

Dehydration of gypsum proceeds via the following steps under atmospheric pressure with increasing temperature: gypsum $CaSO_4.2H_2O$ transforms into β-hemihydrate $CaSO_4.0.5H_2O$ (bassanite) above ~ 110°C, then into γ-anhydrite $CaSO_4$ / anhydrite III (soluble) above ~ 200°C, which transforms into β-anhydrite / anhydrite II (insoluble) above ~ 300°C, and finally into α-anhydrite / anhydrite I (high-temperature phase) above ~ 1200°C [48-50].

The crystal structure of brushite $CaHPO_4.2H_2O$, for a long time considered as isostructural with gypsum, consists of alternate corrugated calcium phosphate layers, perpendicular to the **b** axis, made of zig-zag chains of $CaO_8$ polyhedra linked to zig–zag chains of $PO_4^{3-}$ tetrahedra, parallel to the **a** axis (Fig. 1) [34]. The tetrahedra are connected together via "*strong*" hydrogen bonds (O1-H1---O4, involving the acidic proton H1 (absent in gypsum) belonging to the single -OH group attached to the phosphate units. The structure is less symmetrical than that of gypsum. Water molecules of two different types (unlike gypsum), w1 and w2, form the interlayer, sharing respectively their oxygen with one of the $CaO_8$ polyhedra. They are *weakly* bound together via hydrogen bonds (O3---H2-

O5(w1) and O1---H4-O6(w2)) essentially along the **b** axis. We also note the presence of two other hydrogen bonds: one inside the layers, the intralayer hydrogen bond O3---H3-O5(w1) (also present in gypsum) acting predominantly along the **a** axis, and the other one in the interlayer between the water molecules (w1)O5---H5-O6(w2) along the **c** axis [34] (Table 2).

Thermal decomposition of brushite occurs in three steps: loss of crystallization water (or structural water w1 and w2) in two steps between 110 and 220°C leading to the formation of monetite $CaHPO_4$ (dicalcium phosphate anhydrous DCPA), according to the reaction $CaHPO_4, 2H_2O \rightarrow CaHPO_4 + 2H_2O$ [51]. These two dehydration steps are complete between 200 and 220°C, depending on the heating rate. The third step is the loss of the remaining proton between 320 and 436°C, according to the reaction $CaHPO_4 \rightarrow \gamma\text{-}Ca_2(P_2O_7) + H_2O$, the calcium pyrophosphate $\gamma\text{-}Ca_2(P_2O_7)$ transforming subsequently into $\beta\text{-}Ca_2(P_2O_7)$ at 700°C and into $\alpha\text{–}Ca_2(P_2O_7)$ at 1200°C [34].

Details on the structural models of portlandite and brucite, gypsum and brushite and the hydrogen bonds in gypsum and brushite are summarized in Table 1. Table 2 presents some characteristics of the bonds for brushite, gypsum, portlandite and brucite (OH bond lengths, OHO lengths in case of accepted H-bonding).

### 2.5. Electron irradiations

The NEC Pelletron accelerator of the SIRIUS platform (Ecole Polytechnique, Palaiseau, France) was used for electron irradiation at 2.5 MeV. For each compound, the inelastic stopping power S(E) (in MeV/cm) and range R (in mm) were estimated using the ESTAR code (Table 3). At 2.5 MeV, all electrons pass through the sample, the projected range being in the order of 5 to 6 mm, depending on the mineral. The energy losses in the target, calculated based on the Bethe formula, are substantially identical for all compounds.

Irradiations experiments were conducted under helium gas. The irradiation conditions (flux, current, temperature, dose) chosen for each powder sample are reported in Table 4. Special attention was paid to the temperature control in order to avoid any thermal dehydration, especially in the case of the two water-bearing minerals, gypsum and brushite. The average values of beam current varied between 20 μA and 25 μA for portlandite and brucite. It was the same for gypsum, except for one sample for which a value of 15 μA was imposed to maintain the temperature at 30°C. For brushite, the average beam current was varied over a large range, from 20 μA to 0.5 μA in order to estimate the annealing effects [59]. In order to attain a high dose over a reasonable irradiation time (in the range of one week), a good compromise was found using a beam current in the range of 20 μA. The absorbed dose (in Gy) is calculated as $S(E) \times \Phi/\rho$, with $\rho$ being the density of the mineral. The dose rate $\phi$ and dose $\Phi$ are given in units of absorbed dose in Gray per second (Gy/s) for the first and in GGy for the second respectively.

The displacement damage due to elastic collisions between the incident electron beam and the target nuclei, also called knock-on damage, never exceeds a few $10^{-4}$ dpa for all cations (except hydrogen) and oxygen ions in all four minerals [23, 28], which is in principle insufficient to promote a crystal-to-amorphous transition, referring to [29, 60]. This contribution to the damage is considered negligible by many authors, except otherwise stated when the experiment contradicts the initial hypothesis [10].

## 3. Results and discussion

### 3.1. Main results: radiation damages

The influence/impact of electron irradiation on the structural properties of four OH-bearing layered minerals is here studied by using powder X-ray diffraction essentially. When it is found necessary, additional information obtained by Nuclear Magnetic Resonance spectroscopy is reported to support some of our assumptions. At this point we recall that *(i)* electron irradiation tends to generate isolated defects but no collisions cascades that are considered necessary to cause amorphization of a crystal lattice, and that (ii) the contribution of the ionizing radiation to the overall damage is to be evaluated experimentally for each system. We summarized in Figs. 2-3 and Table 4 the main results of the study as a function of the irradiation conditions. The influence of the dose, and in some cases of the flux or the energy of the electron beam on the damages are analyzed.

As discussed above, portlandite and brucite can be considered *a priori* as simple models for compounds with layered structures, by comparison with gypsum and brushite, which exhibit a complex crystal structure.

#### 3.1.1 Radiation damage in portlandite and brucite

On the basis of the XRD study, portlandite and brucite remain crystalline up to high doses (3-5 GGy), no decomposition into cubic lime CaO for portlandite, nor into periclase MgO for brucite being observed (Fig. 2). Both compounds can be said resistant to electron irradiation as they were found in the past stable under pressure [27]. However, at all doses for the two compounds but more specifically for brucite, an intensity decrease and a broadening of the Bragg peaks are observed with increasing exposure time to the electron beam, concomitant with the appearance of a diffuse scattering over the whole angular range. More precisely, the peak broadening is anisotropic, which may be due to various causes: crystallite size and morphology effects, but also microstrains and lattice defects. Several anisotropic broadening models were tested: the models of Ectors using cylindrical crystallites [62, 63], discussed in [23], and the model for strain broadening proposed by Stephens [64]. In summary, the XRD patterns are correctly refined using both models up to about 100 MGy. For higher doses, above ~ 1 GGy, the pronounced broadening makes (Fig. 3) them useless.

Looking at the diagrams for very high doses, the line profile is characterized by a strong peak shift and an asymmetric and anisotropic line broadening. More precisely, a strong line broadening is found for the 012 and 011 lines (h0l and 0kl lines), but it is very weak for the 010 line. This is compatible with the presence of planar defects often found in lamellar hydroxydes (brucite-type structures like β-$Ni(OH)_2$, $Mg(OH)_2$) and layered double hydroxides (LDHs) [65-70]. Brucite and brucite-type structures are known for their anisotropic peak broadening due to crystal imperfections, and the presence of impurities in the interlayer spacing affecting the shape of some Bragg lines. Consequently, the h0l, 0kl and 00l Bragg lines are naturally affected even in regarded as chemically pure powders (here brucite of 99.7 wt.% purity). More precisely, the 010 planes perpendicular to the layers stacked along the **c** axis are less impacted by stacking faults along this axis, while the 012 and 011 planes are more impacted. The 00l lines are also found broadened, which is explained in the literature by interstratification faults (presence of water molecules or carbonates in the interlayer). We observe here that electron irradiation increases these effects on the diffractograms of the irradiated powders, more in brucite than in portlandite.

### 3.1.2 Radiation damage in gypsum and brushite

By contrast, for the more complex layered structures, gypsum and brushite, and under the same irradiation conditions, electron irradiation causes phase transformations (Fig. 2). Gypsum exhibits a progressive decomposition into less hydrated phases under irradiation, first hemi-hydrate ($CaSO_4.0.5H_2O$) being visible at a dose of 6 MGy, then anhydrite ($\beta$-$CaSO_4$) once reached 400 MGy. We have no proof of the existence of bassanite below 6 MGy, if any only at very low level (typically below 0.5 wt.%). The dehydration of gypsum operates very fast within the range 100 to 400 MGy, then decelerates at higher doses. The full transformation into anhydrite is far from being achieved around 2 GGy, as seen in Fig. 4a, showing the evolution of the chemical composition of the samples with the radiation dose, determined by the Rietveld analysis. The decomposition of gypsum must be attributed solely to an irradiation effect, not to a heating effect, the temperature of the samples being maintained below 36°C, *i.e.* well below the temperature of starting decomposition of gypsum under ambient air (see 2.3.2).

Under the same irradiation conditions, the progressive transformation of brushite into an amorphous phase is evidenced. It was identified as an amorphous calcium pyrophosphate by Raman spectroscopy [28]. A systematic decrease in the intensity of the XRD Bragg lines, and a significant line broadening increase are observed up to 0.12 GGy. For higher doses, the width of the diffraction lines no longer evolves, suggesting that the defect tolerance is reached. As a result of all the data presented in Fig. 2 and Table 4, it appears clearly that not only brushite is very sensitive to 2.5 MeV electron irradiation, but that the defects concentration produced under irradiation invariably leads to the appearance of an amorphous phase. Whatever the flux and dose, no bifurcation towards a decomposed dehydrated state occurs, which could have been the other "natural" microstructural evolution scheme in this temperature range. No monetite was detected by XRD and Raman spectroscopy [28].

If we apply the "direct single peak" method [71] to determine the amorphous fractions of pyrophosphate in the irradiated powders and make a plot as a function of dose (Fig. 4b), we note a change in slope around ~ 0.7 GGy, suggesting a change in the amorphization process, or just a slowing down caused by the local structural evolution of the brushite powder around 0.7 GGy for the applied dose rate ($1.1 \times 10^4$ Gy/s). Interestingly, by characterizing irradiated brushite samples by $^{31}P$ MAS-NMR spectroscopy, Jdaini also noticed a change of regime in the decomposition of brushite at a dose close to 0.7 GGy, above which doubly-bridged metaphosphate ($PO_4$ tetrahedra with two bridging oxygens) started to form [72]. If we superimpose the plots of the phase composition versus dose for brushite and gypsum (inset of Fig. 4b), we notice that it follows the same trend independently of the damage process, amorphization versus decomposition, which was rather unexpected. The reason for that could be the employed technique (appropriate spatial and temporal scales), which masks *real* differences between the damage mechanisms.

As mentioned in Table 4, the effect of dose rate, known to be an important parameter [17], was analyzed, but only for brushite. In order to improve the identification of the diffusion hump, Si wafers were used as zero-background holders. Partial amorphization of brushite is observed whatever the dose rate. All X-ray diffraction lines decrease and broaden whatever the experimental conditions, not only with increasing dose, but also with decreasing dose rate (from $1 \times 10^4$ Gy/s to $3 \times 10^2$ Gy/s) at fixed final dose (~ 210 MGy), high enough to observe some substantial disorder (Fig. 5). We infer that the conclusions of the data analysis presented here (Figs. 2&4) should be independent of the dose rate and that only the value of the amorphization dose for brushite or decomposition dose for gypsum, and the

value of the inflection points on the evolution of the phase composition with dose should possibly shift with the dose rate. Consequently, looking at Fig. 4b, we may suppose that the dose reached at the change in slope would shift towards a lower value with decreasing dose rate. Such prediction could be checked by using an adapted spectroscopy.

### 3.2. Cell volume changes and lattice parameters: irradiation versus heating effects

Following electron irradiation (Fig. 6), the relative volume change ($\Delta V/V$ in %) first increases with increasing radiation dose for all compounds. However, it never attains the level of thermal expansion (~ + 2.5%), reported in the literature over the range of existence of these hydrated compounds (Figs. 7-8) [34, 44-46, 73].

We reported in Figs. 9-11 the relative change in the interlayer lattice parameter, along the c-axis ($\Delta c/c$) for brucite and portlandite and along the b-axis ($\Delta b/b$) for brushite and gypsum as a function of the dose and temperature. There is an effect of the chemistry and microstructure of the sample, but the trends remain the same (Figs. 9&10).

#### 3.2.1 Portlandite and brucite

For the two compounds with simple layered structure, when the dose attains about 1 GGy, a low plateau value is reached: $\Delta V/V$ ~ 1% for brucite and ~ 0.4% for portlandite (Fig. 8). Apparently, the calcite content in portlandite (P1.5, P4, P15) has an effect on the volume expansion. For the "aged" portlandite having the highest $CaCO_3$ content (P15), the plateau value is not attained, but presumably it should not differ significantly from the one attained for the other compounds.

Comparing in more detail the cell dilatation of portlandite and brucite under irradiation (Figs. 9&10), one remarks that it is not exactly the same in these two isostructural compounds. For both, there is a slight increase in unit cell volume with increasing dose, but not in the same way. For portlandite, one observes a dilatation along both **c** and **a** axes, which is anisotropic, being more important along the **c** axis than the **a** axis (Figs. 10a-b). For brucite, there is a dilatation along the **c** axis, larger than for portlandite, sufficient to compensate for the small decrease in the **a** lattice parameter with increasing dose (Figs. 10c-d) and to lead to an overall $\Delta V/V$ increase with dose (Fig. 8). In other words, the unit cells of these two simple isostructural hydroxides are not distorted in the same way under irradiation. This could be possibly justified by a different stacking-fault disorder induced by irradiation in the two compounds. No such effect is seen while heating, simply dilatation along **c** and along **a** axes in the two compounds.

#### 3.2.2 Gypsum and brushite

With increasing the structural complexity, two completely different behaviors are observed. The volume expansion of gypsum is found comparable to that of portlandite and brucite, over the range of investigated doses (Fig. 8). This is not the case for brushite. Under the same irradiation conditions, brushite first expands rapidly with increasing dose, but once reached a very low plateau ($\Delta V/V$ ~ 0.2%) at about 200 MGy, the compound shrinks and seems to recover its initial volume at the highest dose (1.5 GGy). When represented as in Fig. 8, the data clearly show that the irradiation damage cannot be reduced to a simple heating and that the volume expansion caused by electron irradiation is limited by comparison with heating.

Very roughly speaking, the change in the lattice parameters of gypsum within the layer (Δa/a, Δc/c) and in the interlayer (Δb/b) with the radiation dose follows the same trend as for the two studied hydroxides with simple crystalline structure. We note the contraction of Δa/a with increasing dose in gypsum (Fig. 11), to be compared with the contraction effect in the basal plane for brucite (Fig. 10d).

For brushite, not only the dilatation under irradiation is very limited and tends to zero at highest dose, but it seems that the radiation damage is limited to a distortion of the crystal unit cell, leaving quasi unchanged the interlayer at highest dose. In particular, at its maximum, Δb/b reaches the value of + 0.087% at an intermediate dose of about 30 MGy (Fig. 9), to be compared to its maximum value attained upon heating, Δb/b = + 0.77% between 4.2K and 470K [34]. At the same time, Δc/c attains + 0.18% around 210 MGy before coming back to + 0.035% at highest dose, to be compared to its maximum value attained upon heating, Δc/c = + 1.74% between 4.2K and 470K [34], leaving the **c** lattice parameter roughly unchanged after irradiation.

Referring to Fig. 1 and Table 2 in which are listed the five hydrogen bonds in the brushite structure, it is as if the two hydrogen bonds, responsible for the interlayer bonding O3---H2-O5(w1) and O1---H4-O6(w2) bonds parallel to the **b** axis, and the hydrogen bond that forms between the two water molecules w1 and w2 (O5(w1)---H5-O6(w2)) along the **c** axis, were insensitive to electron irradiation.

### 3.2.3 Hydrogen bonding in brushite

We have seen recently by Raman spectroscopy that under comparable electron irradiation conditions, brushite transforms progressively into an amorphous pyrophosphate, with formation of chains of pyrophosphate anions $[P_2O_7]^{4-}$ following the deprotonation of the phosphate tetrahedra inside the chains [28]. This is not inconsistent with a bond breaking occurring inside the layers, and is compatible with the decrease of the **a** lattice parameter seen in Fig. 11 for irradiated brushite.

To check this hypothesis and gain more information on hydrogen bonding in pristine and irradiated brushite, the samples were characterized by $^1$H MAS-NMR spectroscopy. The spectra are presented in Fig. 12, with their assignments.

When the integrated dose increased from 0 to 2.34 GGy, the resonance ascribed to the acidic proton in brushite (10.3 ppm) decreased significantly and almost fully disappeared at the highest irradiation dose, thus confirming the breaking of the strongest hydrogen bond (O4---H1-O1) between the acidic proton and the phosphate group, as inferred from the XRD and Raman results. In contrast, the broad peak associated to molecular $H_2O$ (2.5 – 7.5 ppm) was observed regardless of the integrated dose. This result shows that structural water molecules were not only present in brushite, but also in amorphous calcium pyrophosphate, its degradation product [28]. Besides, from doses of 0.12 GGy onwards, a narrow peak was detected at about 4.2 ppm, with an intensity increasing with the dose. It may correspond to hydrogen gas, produced by water radiolysis, sorbed onto the irradiated solid [75-78] or to a small amount of partly mobile water, adsorbed on the surface or present in micropores of the irradiated solid, and resulting from the decomposition of brushite following the overall equation: $2\ CaHPO_4.2H_2O \rightarrow Ca_2P_2O_7.nH_2O + (5\text{-}n)H_2O$. Similar resonances at chemical shifts in the range 4-5 ppm have already been reported for water exhibiting some mobility in fully hydrated calcium carbonates [79], amorphous calcium phosphates [80] or magnesium sodium phosphate cement pastes [81]. Finally, is it interesting to note that the intensity of the peak at $\delta$ = 15.5 ppm, assigned to the

hydrogen-bonded acidic protons in monetite, which was present as an impurity (2 wt.%) in the investigated brushite sample, did not increase with the irradiation dose. This result thus confirms that irradiation of brushite does not lead to the formation of monetite, unlike an increase in temperature.

To sum up, when one irradiates brushite under low electron flux, the most sensitive bond is the strongest intralayer H bond formed between the acidic proton and the phosphate groups, contrary to what happens upon heating in which case the interlayer H bonds are the most impacted by a temperature increase and the acidic proton is said to play only a minor role in the dehydration mechanism [34].

## 4. Conclusions

For all four H-bearing layered compounds, and under present conditions, electron irradiation causes damages that differ significantly from the ones induced by heating, as it results from the XRD experiments and Rietveld analysis of the diffraction patterns obtained under various irradiation conditions. The difference between electron irradiation and heating is even more marked for the hydrated compounds with complex layered structure (gypsum and brushite) than for the ones with simple layered structures (portlandite and brucite). In other words, the disorder induced by irradiation could be said increasing with the complexity of the crystalline structure.

Portlandite and brucite are found stable under electron irradiation up to doses exceeding a few GGy, and behave in this aspect as the clay minerals studied in the literature [19, 20]. No decomposition into CaO or MgO is observed, but an anisotropic broadening of the Bragg lines, increasing with dose, consistent with a stacking-fault disorder appearing in the crystalline structures, more pronounced in brucite than in portlandite. Further investigations are in progress in order to model the stacking faults disorder.

The more complex layered structures, brushite and gypsum, are much more sensitive to electron irradiation, being subject to phase transformations. Moreover, these two structurally closely related compounds behave differently under irradiation. One observes a partial decomposition of gypsum into less hydrated calcium sulfates, bassanite and anhydrite, whereas brushite progressively transforms into an amorphous calcium pyrophosphate which does not involve the interlayer bonding between water molecules, contrary to what happens thermally.

To our knowledge, this is the first time that amorphization is reported under electron irradiation at low flux. This specific behavior of brushite could be explained by the presence of an acidic proton attached to the phosphate tetrahedra or/and the chemical nature of the tetrahedra forming the chains in the crystalline structure (phosphate in brushite versus sulphate in gypsum). Further investigation is underway in order to investigate the role of the acidic proton in the structural damage process, starting with the study of monetite $CaHPO_4$ with three acidic protons environments and one acidic proton most strongly H-bonded than the two others.

In the light of these results, one should be cautious when using simple layered hydrated compounds, like brucite or portlandite, as model materials to study crystal chemistry of more complex layered hydrated materials.

## Acknowledgements

We thank the SIRIUS team for the support and for the beam time devoted to our investigation. The DIFFRAX facility of Ecole Polytechnique was used for X-Ray measurements. P. Gaveau from Institut Charles Gerhardt Montpellier (ICGM, France) is greatfully acknowledged for NMR measurements. The thanks are also extended to L. Acher and J. Jdaini (CEA) for their contribution to the experimental work.

## References

[1] M. Atkins, F.P. Glasser, Application of Portland cement-based materials to radioactive waste immobilization, Waste Management, 12 (1992) 105-131, https://doi.org/10.1016/0956-053X(92)90044-J.
[2] F. Bart, C. Cau-Dit-Coumes, F. Frizon, S. Lorente, Cement-based materials for nuclear waste storage, (Ed.), Springer, London, 2013.
[3] V. L'Hostis, R. Gens, Performance Assessment of Concrete Structures and Engineered Barriers for Nuclear Applications: Conclusions of RILEM TC 226-CNM, (Ed.), Springer, London, 2016.
[4] A. Hermann, M. Mookherjee, High-pressure phase of brucite stable at Earth's mantle transition zone and lower mantle conditions, PNAS, 113 (2016) 13971-13976, https://doi.org/10.1073/pnas.1611571113.
[5] S.B. Pillai, B. Joseph, P.K. Jha, Brucite ($Mg(OH)_2$) under small perturbation: a combined first principles and synchrotron X-ray diffraction study, Journal of Physics and Chemistry of Solids, 154 (2021) 110078, https://doi.org/10.1016/j.jpcs.2021.110078.
[6] D.T. Vaniman, G.M. Martinez, R.E. B., T.F. Bristow, D.F. Blake, Y.A. S., D.W. Ming, W. Rapin, P.-Y. Meslin, J.M. Morookian, R.T. Downs, S.J. Chipera, R.V. Morris, S.M. Morrison, A.H. Treiman, C.N. Achilles, K. Robertson, J.P. Grotzinger, R.M. Hazen, R.C. Wiens, D.Y. Sumner, Gypsum, bassanite, and anhydrite at Gale crater, Mars, American Mineralogist, 103 (2018) 1011-1020
[7] F.M. Lea, Lea's chemistry of cement and concrete, P. Hewlett, M. Liska (Ed.), Elsevier, New York, 2019.
[8] S.V. Dorozhkin, Synthetic amorphous calcium phosphates (ACPs): preparation, structure, properties, and biomedical applications, Biomaterials Science, 9 (2021) 7748, https://doi.org/10.1039/D1BM01239H.
[9] O. Mishchenko, A. Yanovska, O. Kosinov, D. Maksymov, R. Moskalenko, A. Ramanavicius, M. Pogorielov, Synthetic calcium–phosphate materials for bone grafting, Polymers, 15 (2023) 3822, https://doi.org/10.3390/polym15183822.
[10] V. Aubin-Chevaldonnet, D. Gourier, D. Caurant, S. Esnouf, T. Charpentier, J.-M. Costantini, Paramagnetic defects induced by electron irradiation in barium hollandite ceramics for caesium storage, Journal of Physics: Condensed Matter, 18 (2006) 4007-4027, https://doi.org/10.1088/0953-8984/18/16/009.
[11] V. Aubin-Chevaldonnet, D. Gourier, D. Caurant, J.-M. Costantini, Transformation and clustering of defects induced by electron irradiation in barium hollandite ceramics for radioactive cesium storage: electron paramagnetic resonance study, Journal of Applied Physics, 111 (2012) 083504, https://doi.org/10.1063/1.3702892.
[12] J.-M. Costantini, F. Beuneu, Threshold displacement energy in yttria-stabilized zirconia, Physica Status Solidi, 4 (2007) 1258-1263, https://doi.org/10.1002/pssc.200673752.
[13] J.-M. Costantini, G. Lelong, M. Guillaumet, W.J. Weber, S. Takaki, K. Yasuda, Color-center production and recovery in electron-irradiated magnesium aluminate spinel and ceria, Journal of Physics: Condensed Matter, 28 (2016) 325901, https://doi.org/10.1088/0953-8984/28/32/325901.
[14] K. Medjoubi, R. Cariou, L. Vauche, E. Veinberg-Vidal, C. Jany, C. Rostaing, V. Amalbert, F. Chabuel, B. Boizot, In-situ measurement of the effect of 1-MeV electrons irradiation on III-V//Si at LILT conditions, IEEE Radiation Effects Data Workshop (in conjunction with 2020 NSREC), Santa Fe, NM, USA, (2020), https://doi.org/10.1109/REDW51883.2020.9325850
[15] J.M. Raya-Armenta, N. Bazmohammadi, J.C. Vasquez, J.M. Guerrero, A short review of radiation-induced degradation of III–V photovoltaic cells for space applications, Solar Energy Materials & Solar Cells, 233 (2021) 111379, https://doi.org/10.1016/j.solmat.2021.111379.
[16] M. Hayes, A.M. Stoneham, Defect and defect processes in nonmetallic solids, J.W. Sons (Ed.), New York, 1984.
[17] A. Dunlop, F. Rullier-Albenque, C. Jaouen, C. Templier, J. Davenas, Materials under irradiation, (Ed.), Trans Tech Publications, 1993.
[18] L.M. Wang, J.J. Chen, R.C. Ewing, Radiation and thermal effects on porous and layer structured materials as getters of radionuclides, Current Opinion in Solid State and Materials Science, 8 (2004) 405-418, https://doi.org/10.1016/j.cossms.2005.04.002.
[19] T. Allard, G. Calas, Radiation effects on clay mineral properties, Applied Clay Science, 43 (2009) 143-149, https://doi.org/10.1016/j.clay.2008.07.032.
[20] T. Allard, E. Balan, G. Calas, C. Fourdrin, E. Morichon, S. Sorieul, Radiation-induced defects in clay minerals: a review, Nuclear Instruments & Methods in Physics Research Section B, 277 (2012) 112-120, https://doi.org/10.1016/j.nimb.2011.12.044.

[21] A.P. Shpak, E.A. Kalinichenko, A.S. Lytovchenko, I.A. Kalinichenko, G.V. Legkova, N.N. Bagmut, The effect of γ-irradiation on the structure and subsequent thermal decomposition of brucite, Physics and Chemistry of Minerals, 30 (2003) 59-68, https://doi.org/10.1007/s00269-002-0290-2.
[22] A. Baral, E. Tajuelo Rodriguez, W.A. Hunnicutt, E. Cakmak, H. Sun, J. Ilavsky, Y. Le Pape, T.M. Rosseel, N. Garg, Ultra-high gamma irradiation of calcium silicate hydrates: Impact on mechanical properties, nanostructure, and atomic environments, Cement and Concrete Research, 158 (2022) 106855, https://doi.org/10.1016/j.cemconres.2022.106855.
[23] M.-N. de Noirfontaine, L. Acher, M. Courtial, F. Dunstetter, D. Gorse - Pomonti, An X-ray powder diffraction study of damage produced in $Ca(OH)_2$ and $Mg(OH)_2$ by electron irradiation using the 2.5 MeV SIRIUS accelerator, Journal of Nuclear Materials, 509 (2018) 78-93, https://doi.org/10.1016/j.jnucmat.2018.06.019.
[24] L. Acher, M.-N. de Noirfontaine, D. Chartier, D. Gorse - Pomonti, M. Courtial, S. Tusseau-Nenez, O. Cavani, J. Haas, A. Dannoux-Papin, F. Dunstetter, $H_2$ production under gamma irradiation of a calcium aluminate cement: an experimental study on both cement pastes and its stable hydrates, Radiation Physics and Chemistry, 189 (2021) 109689, https://doi.org/10.1016/j.radphyschem.2021.109689.
[25] P. Laniesse, C. Cau Dit Coumes, G. Le Saout, A. Mesbah, Understanding the setting and hardening process of wollastonite-based brushite cement. Part 1: Influence of the Ca/P ratio and $H_3PO_4$ concentration of the mixing solution, Cement and Concrete Research, 134 (2020) 106094, https://doi.org/10.1016/j.cemconres.2020.106094.
[26] Y. Fei, H.-K. Mao, Static compression of $Mg(OH)_2$ to 78 GPa at high temperature and constraints on the equation of state of fluid $H_2O$, Journal of Geophysical Research, 98 (1993) 11875-11884, https://doi.org/10.1029/93JB00701.
[27] M.B. Kruger, Q. Williams, R. Jeanloz, Vibrational spectra of $Mg(OH)_2$ and $Ca(OH)_2$ under pressure, Journal of Chemical Physics, 91 (1989) 5910-5915, https://doi.org/10.1063/1.457460.
[28] M.-N. de Noirfontaine, E. Garcia-Caurel, D. Funes-Hernando, M. Courtial, S. Tusseau-Nenez, O. Cavani, J. Jdaini, C. Cau-Dit-Coumes, F. Dunstetter, D. Gorse - Pomonti, Amorphization of a proposed sorbent of strontium, brushite, $CaHPO_4•2H_2O$, studied by X-ray diffraction and Raman spectroscopy, Journal of Nuclear Materials, 545 (2021) 152751, https://doi.org/10.1016/j.jnucmat.2020.152751.
[29] W.J. Weber, R.C. Ewing, C.R.A. Catlow, T. Diaz de la Rubia, L.W. Hobbs, C. Kinoshita, H. Matzke, A.T. Motta, M. Nastasi, E.K.H. Salje, E.R. Vance, S.J. Zinkle, Radiation effects in crystalline ceramics for the immobilization of high-level nuclear waste and plutonium, Journal of Materials Research, 13 (1998) 1434-1484, https://doi.org/10.1557/JMR.1998.0205.
[30] W.A. Dollase, Correction of intensities for preferred orientation in powder diffractometry: application of the March Model, Journal of Applied Crystallography, 19 (1986) 267-272, https://doi.org/10.1107/S0021889886089458.
[31] O. Chaix-Pluchery, J. Pannetier, J. Bouillot, J.C. Niepce, Structural prereactional transformations in $Ca(OH)_2$, Journal of Solid State Chemistry, 67 (1987) 225-234, https://doi.org/10.1016/0022-4596(87)90358-6.
[32] M. Catti, G. Ferraris, S. Hull, A. Pavese, Static compression and H disorder in brucite, $Mg(OH)_2$, to 11 GPa: a powder neutron diffraction study, Physics and Chemistry of Minerals, 22 (1995) 200-206, https://doi.org/10.1007/BF00202300.
[33] A.G. de la Torre, M.-G. Lopez-Olmo, C. Alvarez-Rua, S. Garcia-Granda, M.A.G. Aranda, Structure and microstructure of gypsum and its relevance to Rietveld quantitative phase analyses, Powder Diffraction, 19 (2004) 240-246, https://doi.org/10.1154/1.1725254.
[34] P.F. Schofield, K.S. Knight, J.A.M. van der Houwen, E. Valsami-Jones, The role of hydrogen bonding in the thermal expansion and dehydration of brushite, di-calcium phosphate dihydrate, Physics and Chemistry of Minerals, 31 (2004) 606-624, https://doi.org/10.1007/s00269-004-0419-6.
[35] C. Bezou, A.N. Christensen, D. Cox, M. Lehmann, A. Nonat, Crystalline structures of $CaSO_4$, 0.5 $H_2O$ and $CaSO_4$, 0.6 $H_2O$, Comptes Rendus de l'Académie des Sciences de Paris, 312 (1991) 43-48, https://doi.org/10.1006/jssc.1995.1260.
[36] G.C.H. Cheng, J. Zussman, The crystal structure of anhydrite ($CaSO_4$), Acta Crystallographica, 16 (1963) 767-769, https://onlinelibrary.wiley.com/doi/abs/10.1107/S0365110X63001997.
[37] K.J.D. MacKenzie, M.E. Smith, Multinuclear solid-state nuclear magnetic resonance of inorganic materials, Pergamon (Ed.), 1st edition. Elsevier Science, London, 2002.
[38] J. Feng, J.A. Reimer, Suppression of probe background signals via $B_1$ field inhomogeneity, Journal of Magnetic Resonance, 209 (2011) 300-305, https://doi.org/10.1016/j.jmr.2011.01.023.
[39] K. Momma, F. Izumi, VESTA 3 for three-dimensional visualization of crystal, volumetric and morphology data, Journal of Applied Crystallography, 44 (2011) 1272-1276, http://dx.doi.org/10.1107/S0021889811038970.
[40] W.R. Busing, H.A. Levy, Neutron diffraction study of calcium hydroxide, The Journal of Chemical Physics, 26 (1957) 563-568, https://doi.org/10.1063/1.1743345.
[41] J.D. Bernal, H.D. Megaw, The function of hydrogen in intermolecular forces, Proceedings of the Royal Society A, 151 (1935) 384, https://doi.org/10.1098/rspa.1935.0157.
[42] L. Desgranges, D. Grebille, G. Calvarin, G. Chevrier, N. Floquet, J.C. Niepce, Hydrogen thermal motion in calcium hydroxide: $Ca(OH)_2$, Acta Crystallographica Section B, 49 (1993) 812-817, https://doi:10.1107/S0108768193003556.

[43] L. Desgranges, G. Calvarin, G. Chevrier, Interlayer interactions in $M(OH)_2$: a neutron diffraction study of $Mg(OH)_2$, Acta Crystallographica B, 52 (1996) 82-86, https://doi.org/10.1107/S0108768195008275.
[44] H. Xu, Y. Zhao, S.C. Vogel, L.L. Daemen, D.D. Hickmott, Anisotropic thermal expansion and hydrogen bonding behavior of portlandite: a high-temperature neutron diffraction study, Journal of Solid State Chemistry, 180 (2007) 1519-1525, https://doi.org/10.1016/j.jssc.2007.03.004.
[45] H. Xu, Y. Zhao, D.D. Hickmott, N.J. Lane, S.C. Vogel, J. Zhang, L.L. Daemen, High-temperature neutron diffraction study of deuterated brucite, Physics and Chemistry of Minerals, 40 (2013) 799-810, https://doi.org/10.1007/s00269-013-0614-4.
[46] P.F. Schofield, K.S. Knight, I.C. Stretton, Thermal expansion of gypsum investigated by neutron powder diffraction, American Mineralogist, 81 (1996) 847-851, https://doi.org/10.2138/am-1996-7-807.
[47] P.F. Henry, M.T. Weller, C.C. Wilson, Neutron powder diffraction in materials with incoherent scattering: an illustration of Rietveld refinement quality from nondeuterated gypsum, Journal of Applied Crystallography, 42 (2009) 1176-1188, https://doi.org/10.1107/S0021889809043210.
[48] S.D.M. Jacques, A. Gonzalez-Saborido, O. Leynaud, J. Bensted, M. Tyrer, R.I.W. Greaves, P. Barnes, Structural evolution during the dehydration of gypsum materials, Mineralogical Magazine, 73 (2009) 421-432, https://doi.org/10.1180/minmag.2009.073.3.42.
[49] L. Ritterbach, P. Becker, Temperature and humidity dependent formation of $CaSO_4 \cdot xH_2O$ (x = 0...2) phases, Global and Planetary Change, 187 (2020) 103132, https://doi.org/10.1016/j.gloplacha.2020.103132.
[50] T. Schmid, R. Jungnickel, P. Dariz, Insights into the $CaSO_4$–$H_2O$ system: a Raman-spectroscopic study, Minerals, 10 (2020) 115, https://doi.org/10.3390/min10020115.
[51] R.L. Frost, S.J. Palmer, Thermal stability of the 'cave' mineral brushite $CaHPO_4 \cdot 2H_2O$ – Mechanism of formation and decomposition, Thermochimica Acta, 521 (2011) 14-17, https://doi.org/10.1016/j.tca.2011.03.035.
[52] S. Raugei, P.L. Silverstrelli, M. Parrinello, Pressure-induced frustration and disorder in $Mg(OH)_2$ and $Ca(OH)_2$, Physical Review Letters, 83 (1999) 2222-2025, https://doi.org/10.1103/PhysRevLett.83.2222.
[53] P. d'Arco, M. Causa, C. Roetti, B. Silvi, Periodic Hartree-Fock study of a weakly bonded layer structure: brucite $Mg(OH)_2$, Physical Review B, 47 (1993) 3522-3529, https://doi.org/10.1103/PhysRevB.47.3522.
[54] B.C. Chakoumakos, C.-K. Loong, A.J. Schultz, Low-temperature structure and dynamics of brucite, Journal of Physical Chemistry B, 101 (1997) 9458-9462, https://doi.org/10.1021/jp972225a.
[55] W.F. Cole, C.J. Lankucki, A refinement of the crystal structure of gypsum $CaSO_4.2H_2O$, Acta Crystallographica B, 30 (1974) 921-929, https://doi.org/10.1107/S0567740874004055.
[56] M. Atoji, R.E. Rundle, Neutron diffraction study of gypsum, $CaSO_42H_2O$, The Journal of Chemical Physics, 29 (1958) 1306-1311, https://doi.org/10.1063/1.1744713.
[57] N.A. Curry, D.W. Jones, Crystal structure of brushite, calcium hydrogen orthophosphate dihydrate: a neutron-diffraction investigation, Journal of the Chemical Society A, 0 (1971) 3725-3729, https://doi.org/10.1039/J19710003725.
[58] L. Tortet, J.R. Gavarri, G. Nihoul, A.J. Dianoux, Study of protonic mobility in $CaHPO_4 \cdot 2H_2O$ (Brushite) and $CaHPO_4$ (Monetite) by infrared spectroscopy and neutron scattering, Journal of Solid State Chemistry, 132 (1997) 06-16, https://doi.org/10.1006/jssc.1997.7383.
[59] J. Lefèvre, J.-M. Costantini, S. Esnouf, G. Petite, Silicon threshold displacement energy determined by photoluminescence in electronirradiated cubic silicon carbide, Journal of Applied Physics, 105 (2009) 023520, https://doi.org/10.1063/1.3072681.
[60] W.J. Weber, Models and mechanisms of irradiation-induced amorphization in ceramics, Nuclear Instruments & Methods in Physics Research Section B, 166-167 (2000) 98-106, https://doi.org/10.1016/S0168-583X(99)00643-6.
[61] M.J. Berger, J.S. Coursey, M.A. Zucker, J. Chang, Stopping-power and range tables for electrons, protons, and helium ions, NIST, Physical Measurement Laboratory, IUCR Report 37 and 49 (1984), http://www.nist.gov/pml/data/star/.
[62] D. Ectors, F. Goetz-Neuhoeffer, J. Neubauer, A generalized geometric approach to anisotropic peak broadening due to domain morphology, Journal of Applied Crystallography, 48 (2015) 189-194, https://doi.org/10.1107/S1600576714026557.
[63] D. Ectors, F. Goetz-Neuhoeffer, J. Neubauer, Routine (an)isotropic crystallite size analysis in the double-Voigt approximation done right?, Powder Diffraction, 32 (2017) S27-S34, https://doi.org/10.1017/S0885715617000070.
[64] P.W. Stephens, Phenomenological model of anisotropic peak broadening in powder diffraction, Journal of Applied Crystallography, 32 (1999) 281-289, http://dx.doi.org/10.1107/S0021889898006001.
[65] A.V. Radha, P.V. Kamath, G.N. Subbanna, Disorder in layered hydroxides: synthesis and DIFFaX simulation studies of $Mg(OH)_2$, Materials Research Bulletin, 38 (2003) 731-740, https://doi.org/10.1016/S0025-5408(03)00070-9.
[66] G.S. Thomas, P.V. Kamath, Line broadening in the PXRD patterns of layered hydroxides: the relative effects of crystallite size and structural disorder, Journal of Chemical Sciences, 118 (2006) 127-133, https://doi.org/10.1007/BF02708774.

[67] A.V. Radha, P.V. Kamath, C. Shivakumara, Order and disorder among the layered double hydroxides: combined Rietveld and DIFFaX approach, Acta Crystallographica B, 63 (2007) 243-250, https://doi.org/10.1107/S010876810700122X.
[68] T.N. Ramesh, P.V. Kamath, Planar defects in layered hydroxides: simulation and structure refinement of β-nickel hydroxide, Materials Research Bulletin, 43 (2008) 3227-3233, https://doi.org/10.1016/j.materresbull.2008.02.024.
[69] S. Bette, B. Hinrichsen, D. Pfister, E. Dinnebier, A routine for the determination of the microstructure of stacking-faulted nickel cobalt aluminium hydroxide precursors for lithium nickel cobalt aluminium oxide battery materials, Journal of Applied Crystallography, 53 (2020) 76-87, https://doi.org/10.1107/S1600576719016212.
[70] D. Jansen, A. German, D. Ectors, F. Winnefeld, Stacking faults of the hydrous carbonate-containing brucite (HCB) phase in hydrated magnesium carbonate cements, Cement and Concrete Research, 175 (2024) 107371, https://doi.org/10.1016/j.cemconres.2023.107371.
[71] I.C. Madsen, N.V.Y. Scarlett, A. Kern, Description and survey of methodologies for the determination of amorphous content via X-ray powder diffraction, Zeitschrift für Kristallographie, 226 (2011) 944-955, https://doi.org/10.1524/zkri.2011.1437.
[72] J. Jdaini, Potentialités des ciments brushitiques pour le traitement et le conditionnement de déchets radioactifs contaminés par du strontium, in, Ecole Nationale Supérieure de Chimie de Montpellier, France, 2022.
[73] B.C. Chakoumakos, J. Horita, V.O. Garlea, H/D isotope effects in brucite at low temperatures, American Mineralogist, 98 (2013) 1-6, https://doi.org/10.2138/am.2013.4202.
[74] A. Lucas, M. Mouallem-Bahout, C. Carel, J. Gaudé, M. Matecki, Thermal expansion of synthetic aragonite condensed review of elastic properties, Journal of Solid State Chemistry, 146 (1999) 73-78, https://doi.org/10.1006/jssc.1999.8310.
[75] J. Lu, Z.Z. Fang, H.Y. Sohn, R.C. Bowman, S.-J. Hwang, Potential and reaction mechanism of Li-Mg-Al-N-H system for reversible hydrogen storage, The Journal of Physical Chemistry C, 111 (2007) 16686-16692, https://doi.org/10.1021/jp074814e.
[76] C. Lu, J. Hu, J.H. Kwak, Z. Yang, R. Ren, T. Markmaitree, L.L. Shaw, Study the effects of mechanical activation on Li–N–H systems with 1 H and 6 Li solid-state NMR, Journal of Power Sources, 170 (2007) 419-424, https://doi.org/10.1016/j.jpowsour.2007.02.080.
[77] L.J. Florusse, C.J. Peters, J. Schoonman, K.C. Hester, C.A. Koh, S.F. Dec, K.N. Marsh, E.D. Sloan, Stable low-pressure hydrogen clusters stored in a binary clathrate hydrate, Science, 306 (2004) 469-471, https://doi.org/10.1126/science.1102076.
[78] D.V. Bavykin, J.M. Friedrich, F.C. Walsh, Protonated titanates and $TiO_2$ nanostructured materials: synthesis, properties, and applications, Advanced Materials, 18 (2006) 2807-2824, https://doi.org/10.1002/adma.200502696.
[79] J. Ihli, W.C. Wong, E.H. Noel, Y.-Y. Kim, A.N. Kulak, H.K. Christenson, M.J. Duer, F.C. Meldrum, Dehydration and crystallization of amorphous calcium carbonate in solution and in air, Nature Communications, 5 (2014) 3169, https://doi.org/10.1038/ncomms4169.
[80] C. Jaeger, S. Maltsev, A. Karrasch, Progress of structural elucidation of amorphous calcium phosphate(ACP)and hydroxyapatite (HAp): disorder and surfaces as seen by solid state NMR, Key Engineering Materials, 309-311 (2006) 69-72, https://doi.org/10.4028/www.scientific.net/KEM.309-311.69.
[81] K. Sotiriadis, P. Macova, A.S. Mazur, P.M. Tolstoy, A. Viani, A solid state NMR and in-situ infrared spectroscopy study on the setting reaction of magnesium sodium phosphate cement, Journal of Non-Crystalline Solids, 498 (2018) 49-59, https://doi.org/10.1016/j.jnoncrysol.2018.06.006.
[82] J.P. Yesinowski, H. Eckert, Hydrogen environments in calcium phosphates: $^{1}H$ MAS NMR at high spinning speeds, Journal of the American Chemical Society, 109 (1987) 6274-6282, https://doi.org/10.1021/ja00255a009.
[83] J.P. Yesinowski, Nuclear Magnetic Resonance spectroscopy of calcium phosphates, in: Z. Amjad (Ed.) Calcium Phosphates in Biological and Industrial Systems, Springer, New York, 1998, pp. https://doi.org/10.1007/978-1-4615-5517-9
[84] A. Kaflak-Huchulska, A. Samoson, W. Kolodziejski, $^{1}H$ MAS and $^{1}H \rightarrow {}^{31}P$ CP/MAS NMR study of human bone mineral, Calcified Tissue International, 73 (2003) 476-486, https://doi.org/10.1007/s00223-002-2111-5.
[85] F. Pourpoint, C. Gervais, L. Bonhomme-Coury, T. Azaïs, C. Coelho, F. Mauri, B. Alonso, F. Babonneau, C. Bonhomme, Calcium phosphates and hydroxyapatite: solid-state NMR experiments and first-principles calculations, Applied Magnetic Resonance, 32 (2007) 435-457, https://doi.org/10.1007/s00723-007-0040-1.
[86] X. Xue, M. Kanzaki, Proton distributions and hydrogen bonding in crystalline and glassy hydrous silicates and related inorganic materials: insights from high- resolution solid-state nuclear magnetic resonance spectroscopy, Journal of the American Ceramic Society, 92 (2009) 2803-2830, https://doi.org/10.1111/j.1551-2916.2009.03468.x.
[87] Y. Yu, B. Stevensson, M. Pujari-Palmer, H. Guo, H. Engqvist, M. Eden, The monetite structure probed by advanced solid-state NMR experimentation at fast magic-angles spinning, International Journal of Molecular Sciences, 20 (2019) 6356, https://doi.org/10.3390/ijms20246356.

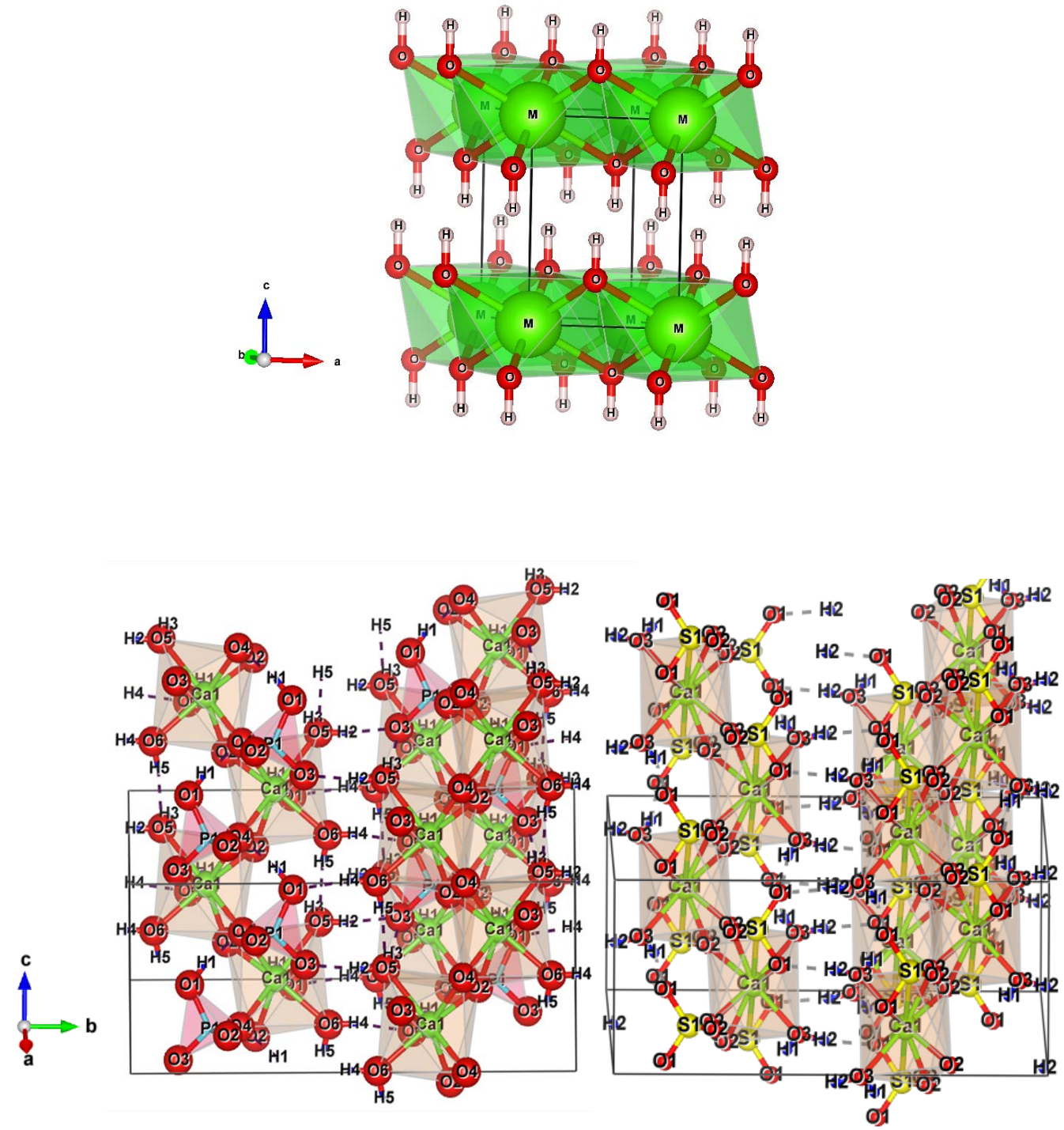


**Fig. 1.** Schematic representation (VESTA software [39]) of the crystal structures: (top) trigonal structure of $M(OH)_2$ hydroxides, with M (metal cation) = Ca, Mg within the one-site hydrogen model [31, 32]; (bottom left) gypsum *$CaSO_4.2H_2O$ [33] and* (bottom right) brushite *$CaHPO_4.2H_2O$ [34]*. The structure of brushite is less symmetrical than that of gypsum. The H atoms are numbered H1 to H2 for gypsum and H1 to H5 for brushite. The Ca atoms are shaded light green at the center of the $CaO_8$ polyhedra with the O atoms in red numbered O1 to O3 for gypsum and O1 to O6 for brushite. The main difference between brushite and gypsum comes from the acidic proton H1 associated to the phosphate groups in brushite, absent in gypsum. Water molecules are of two types in brushite referred to as w1 (H2-O5-H3) and w2 (H4-O6-H5), unlike of one type in gypsum referred to as H1-O3-H2.

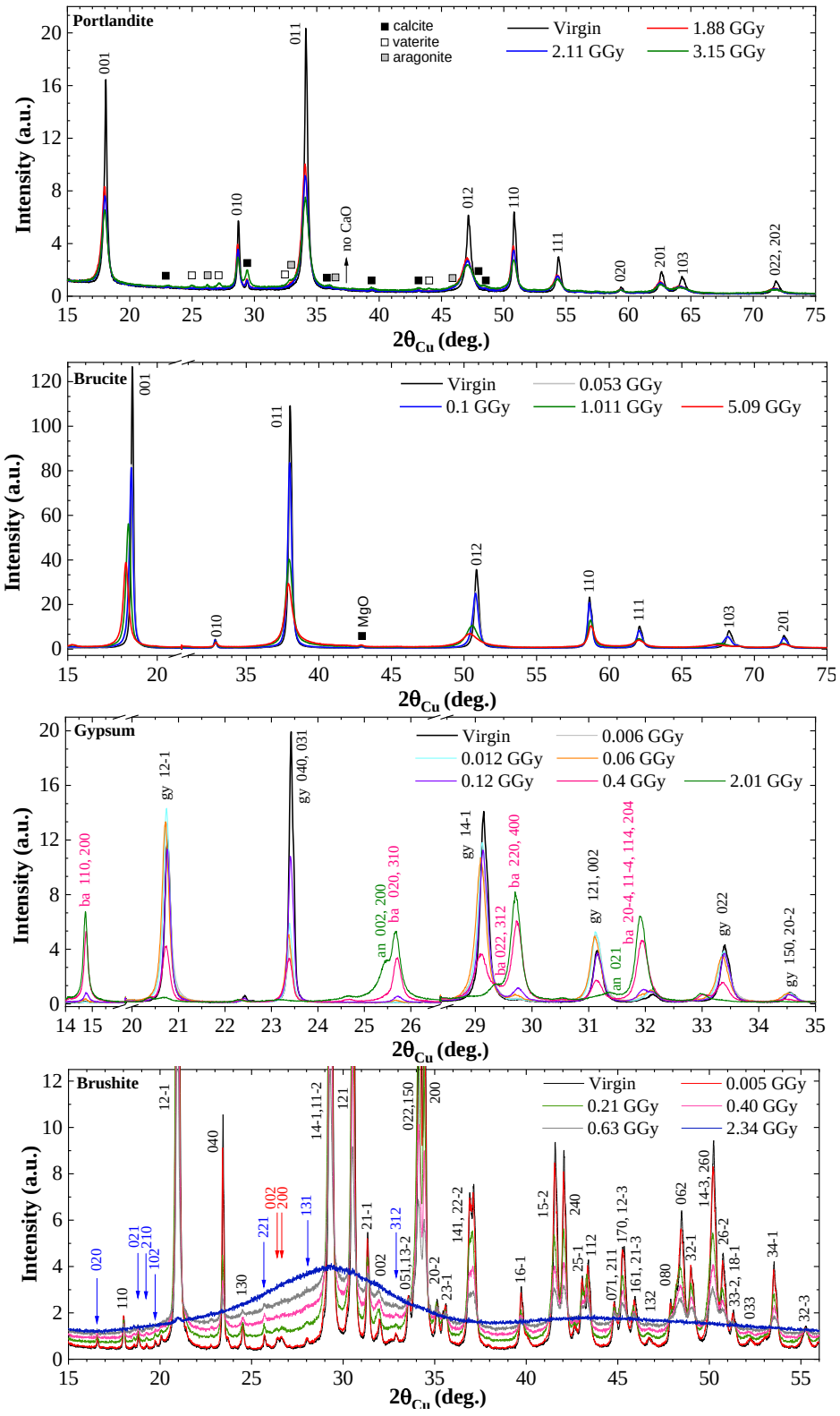


**Fig. 2.** XRD raw data of portlandite (P1.5 sample), brucite (B-PRO sample), gypsum and brushite, as a function of the irradiation dose (in GGy), revealing: a) the stability of portlandite and brucite under electron irradiation, b) the decomposition of gypsum into bassanite and anhydrite with increasing dose, c) the transformation of brushite into an amorphous pyrophosphate, starting in the early stages of irradiation. For portlandite, the most irradiated sample contains 7.3 wt.% calcite (black square) and two other polymorphs of $CaCO_3$: 3.9 wt.% vaterite (white square) and 2.6 wt.% aragonite (grey square), resulting from sample storage conditions. For XRD patterns of gypsum, the hkl Bragg lines are in black for gypsum ("gy"), in pink for bassanite ("ba") and in green for anhydrite ("an"). For brushite, the reflections are indicated in black for brushite, in red for monetite and in blue for newberyte.

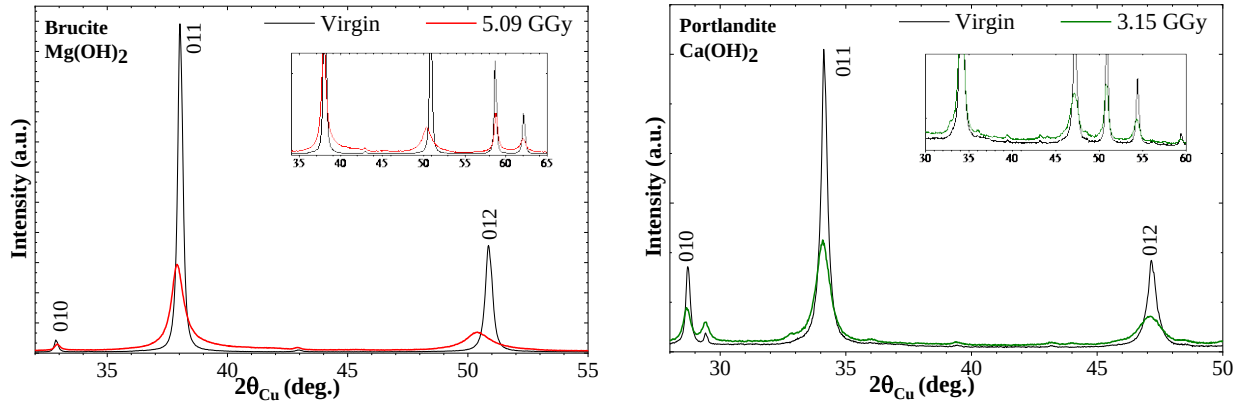


**Fig. 3.** XRD raw data of brucite (B-PRO sample) and portlandite (P1.5 sample) irradiated at very high doses, showing peak shift, anisotropic and asymmetric peak broadening (see 012 and 011 lines, contrast to 010 line) that merges with the background, more pronounced in brucite than in portlandite.

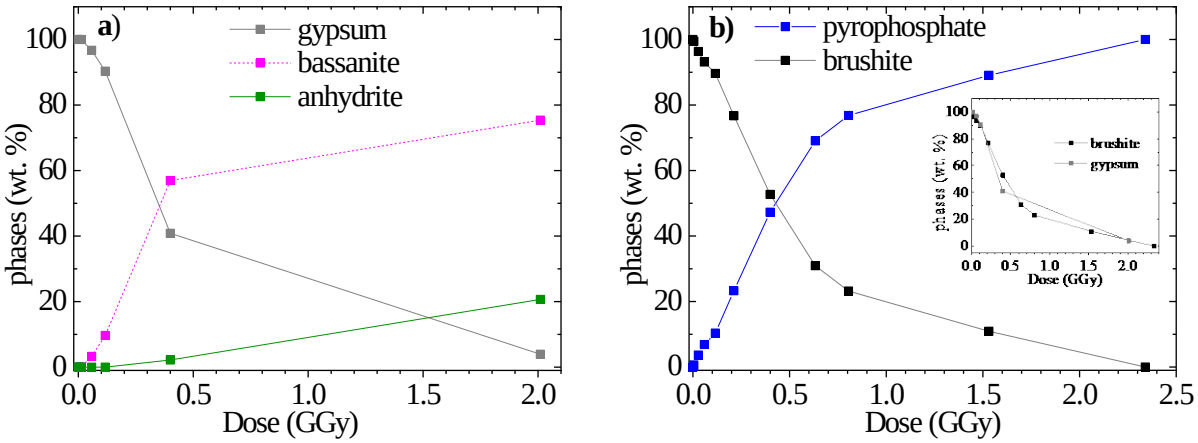


**Fig. 4.** Phase compositions deduced from XRD data. (a) Decomposition products of gypsum (deduced from Rietveld analysis) following electron irradiation at high doses. (b) Plot of the amorphous pyrophosphate content versus dose, revealing a net change in slope around 0.7 GGy. In inset, the evolution of the specimen compositions with dose are superimposed.

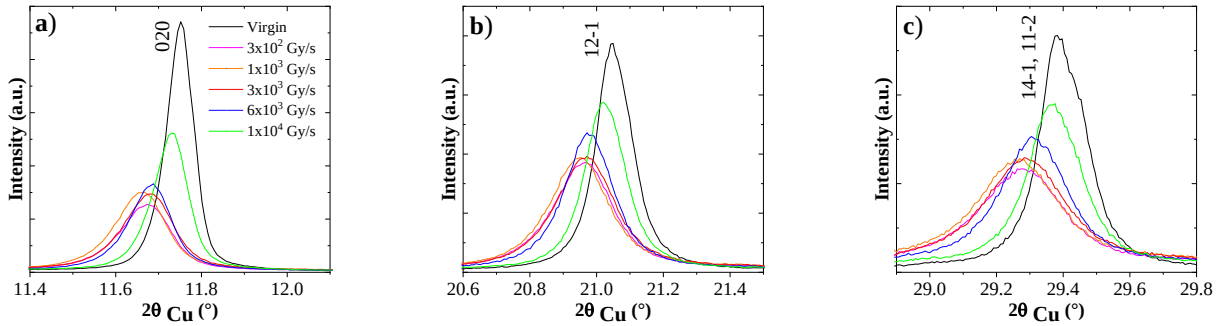


**Fig. 5.** Effect of dose rate on XRD line broadening for irradiated brushites at 210 MGy from 1 x $10^4$ Gy/s (20 µA) to 3 x $10^2$ Gy/s (0.5 µA). Below 3 x $10^3$ Gy/s (5 µA), the flux effect is no longer visible, a plateau is reached, the width of the diffraction lines no longer evolves.

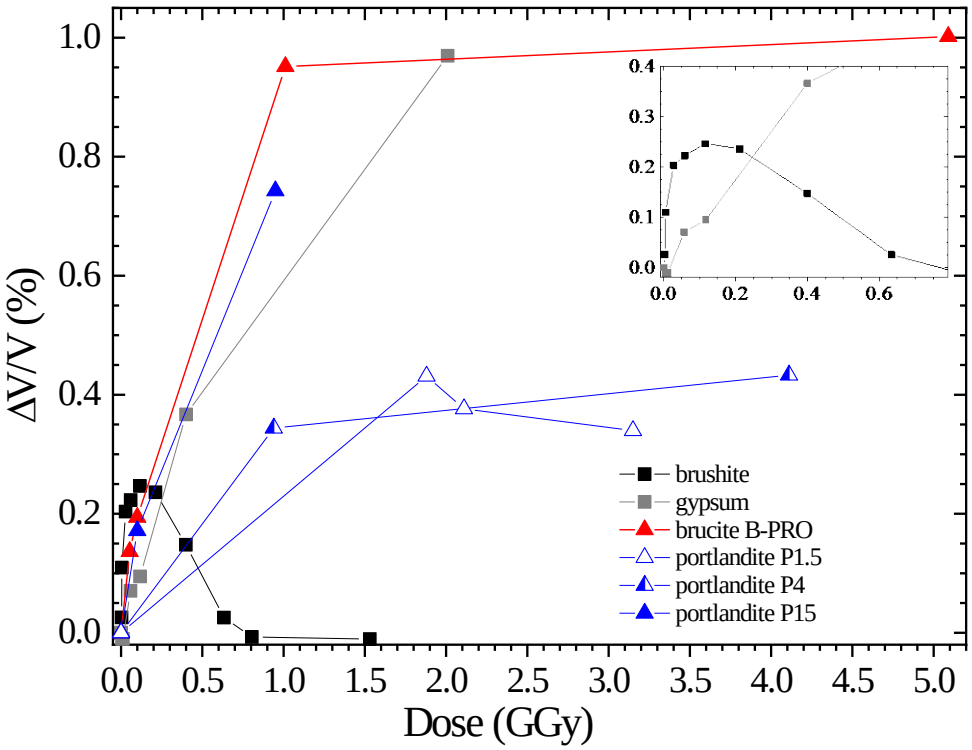


**Fig. 6.** Relative cell volume changes ΔV(%) = [($V_{dose}$ – $V_{virgin}$)/$V_{virgin}$] x 100 versus dose (GGy) calculated post-irradiation for various compounds, showing an increasing expansion, going from portlandites P1.5, P4 and P15 with increasing content of initial calcite (1.5 to 15 wt.%), gypsum, and finally to brucite (B-PRO). We note a significant shrinkage of brushite following a rapid initial volume expansion. The remarkable change in behavior between brushite and gypsum, considered isotructural in the literature, is highlighted in the inset.

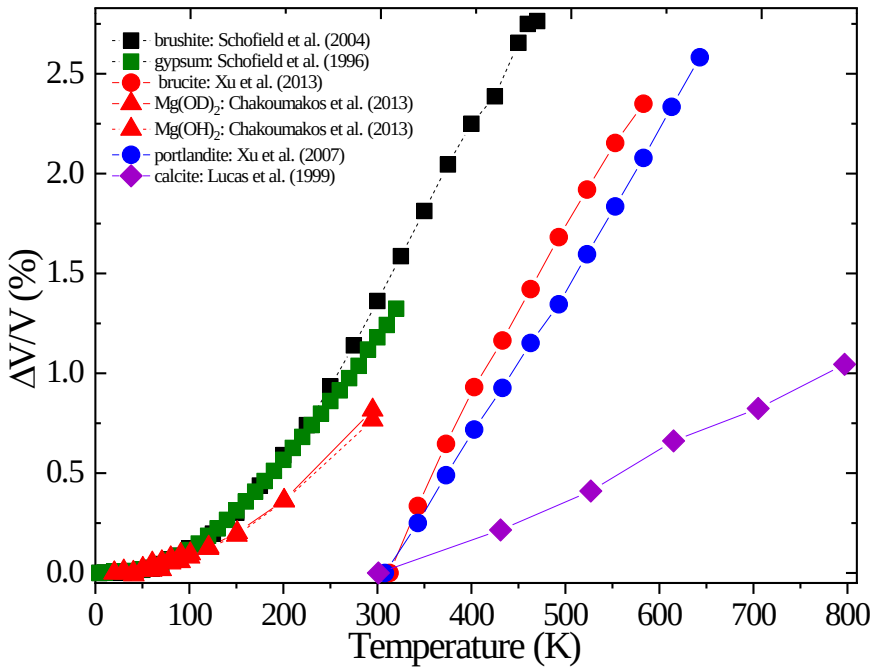


**Fig. 7.** Relative volume changes (%) versus temperature (K) for the compounds (deuterated compounds) considered, after the literature data from *in-situ* neutron diffraction studies [34, 44-46, 73, 74], showing a general volume expansion, and in all cases, largely more significant than above in Fig. **6**. For brucite, the isotopic effect (H/D) is also reported for the low temperature range by [73].

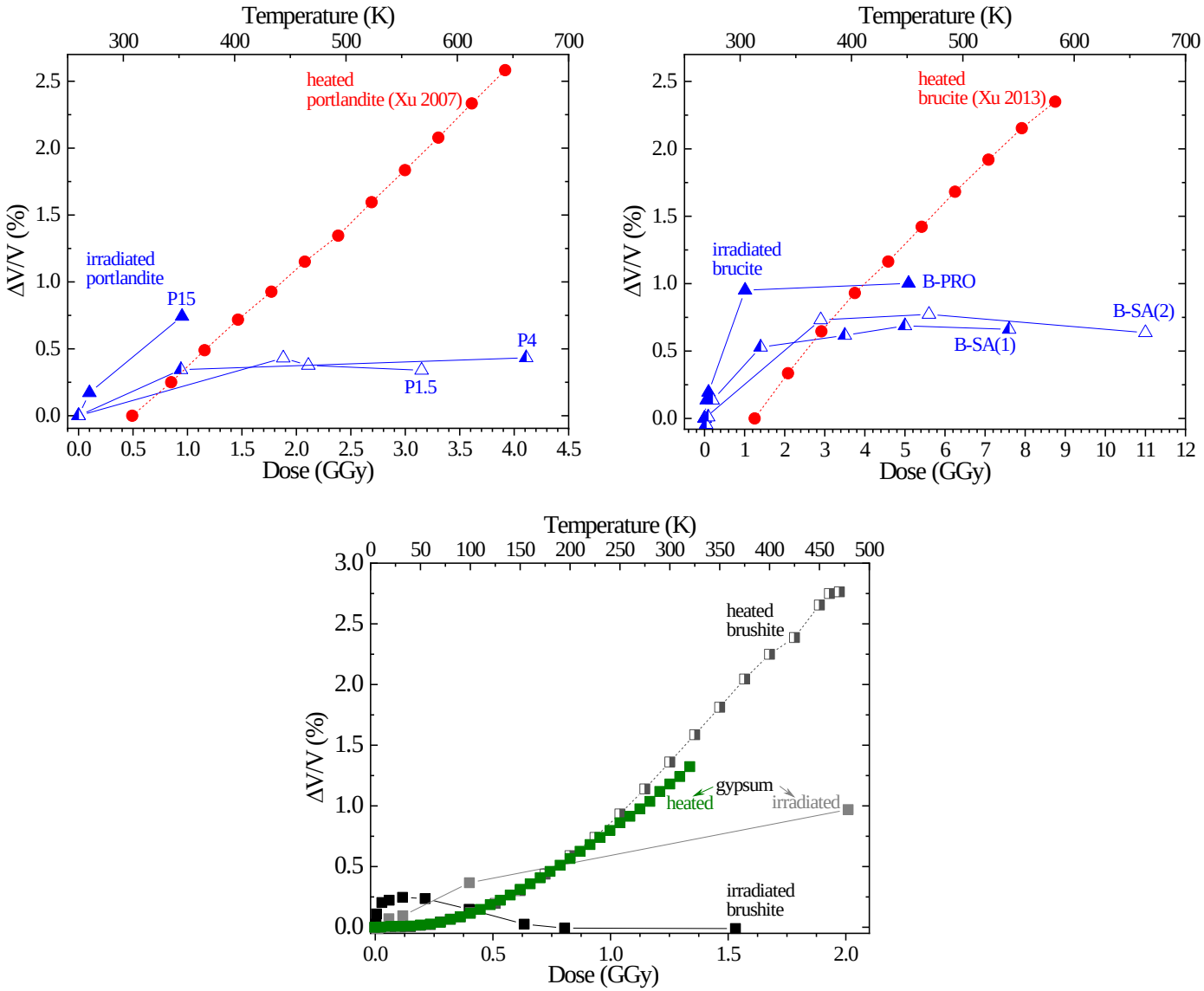


**Fig. 8.** *Top left:* Relative volume changes (%) versus dose (GGy) in lower scale and versus temperature (K) in upper scale for portlandite samples irradiated (P1.5, P4 and P15) or heated [44]. *Top right*: same for brucite samples (B-PRO, B-SA(1) and B-SA(2)) [45]; *Bottom*: same for gypsum [46] and brushite [34], both irradiated or heated. These plots clearly show that the irradiation damage cannot be reduced to a simple heating and that the volume expansion observed under electron irradiation is not only very limited, but decreases with increasing the structural complexity of the layers: going from simple sheets of $Mg(OH)_6$ octahedra for brucite to the complex sheets made of $CaO_8$ polyhedra and sulfate or phosphate tetrahedra for gypsum or brushite.

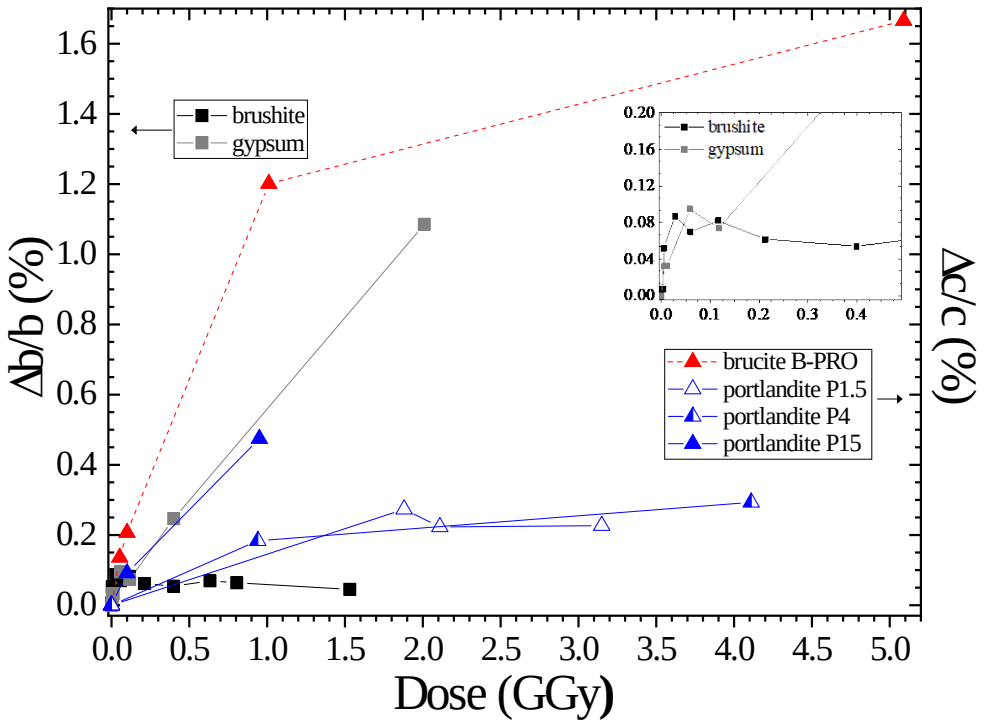


**Fig. 9.** Relative interlayer lattice parameter change versus dose (GGy): *Left scale:* Δb/b (%) for gypsum and brushite; *Right scale*: Δc/c (%) for brucite (B-PRO) and portlandite with various calcite contents (P1.5, P4 and P15). In inset, note the comparable change in lattice parameter Δb/b for gypsum and brushite up to about 100 MGy, characterized by only a shift in dose, followed by an abrupt change in behavior, with gypsum behaving like compounds with simple layered structure (brucite and portlandite) contrary to brushite exhibiting a "singular" behavior recovering roughly its initial lattice parameter at high dose.

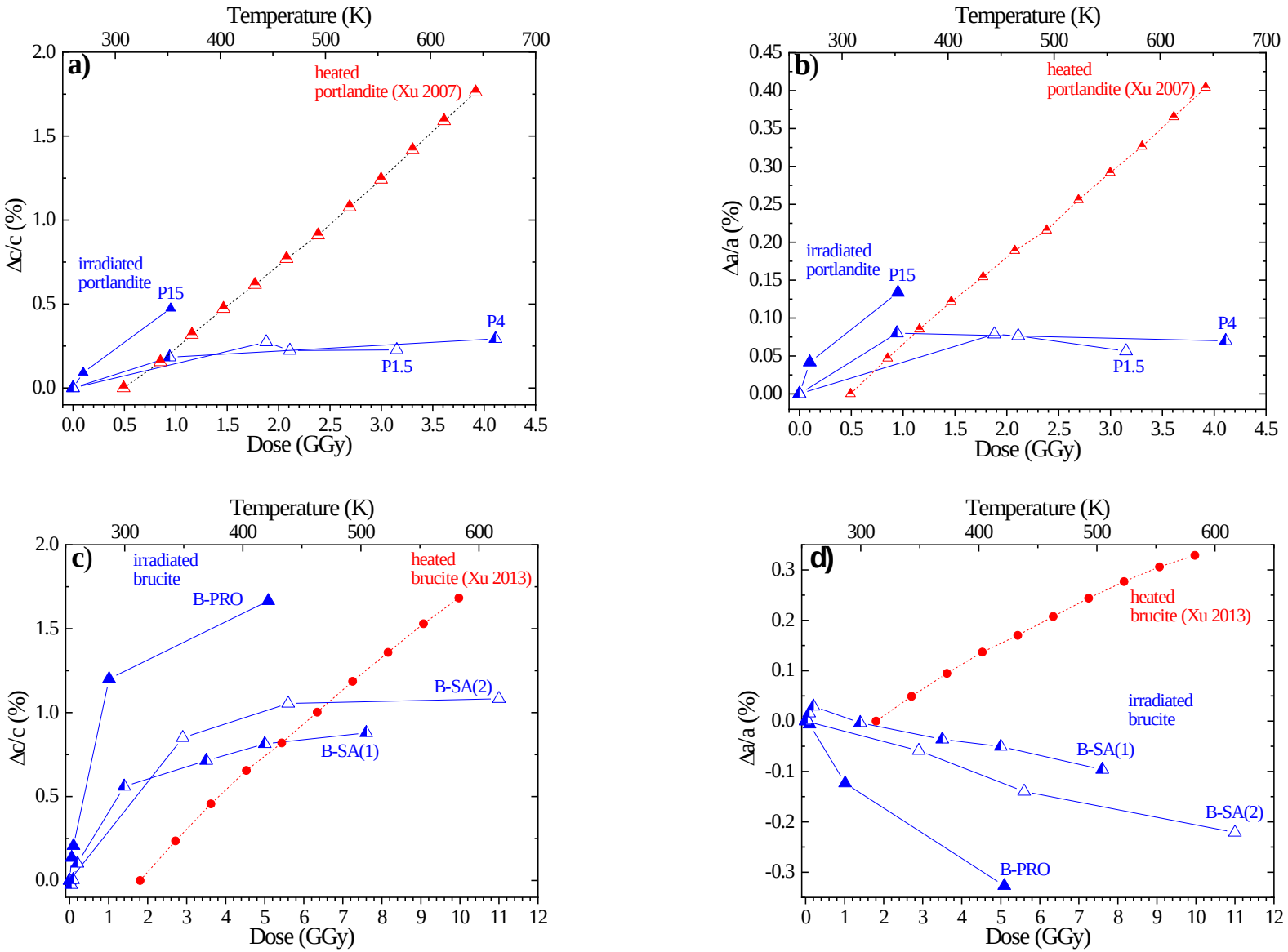


**Fig. 10.** (a-b) Relative unit cell parameters (Δc/c and Δa/a in %) for portlandite with various calcite contents (P1.5, P4 and P15 samples) versus dose (bottom scale) and temperature (top scale) [44]; (c,d): same for brucite [45].

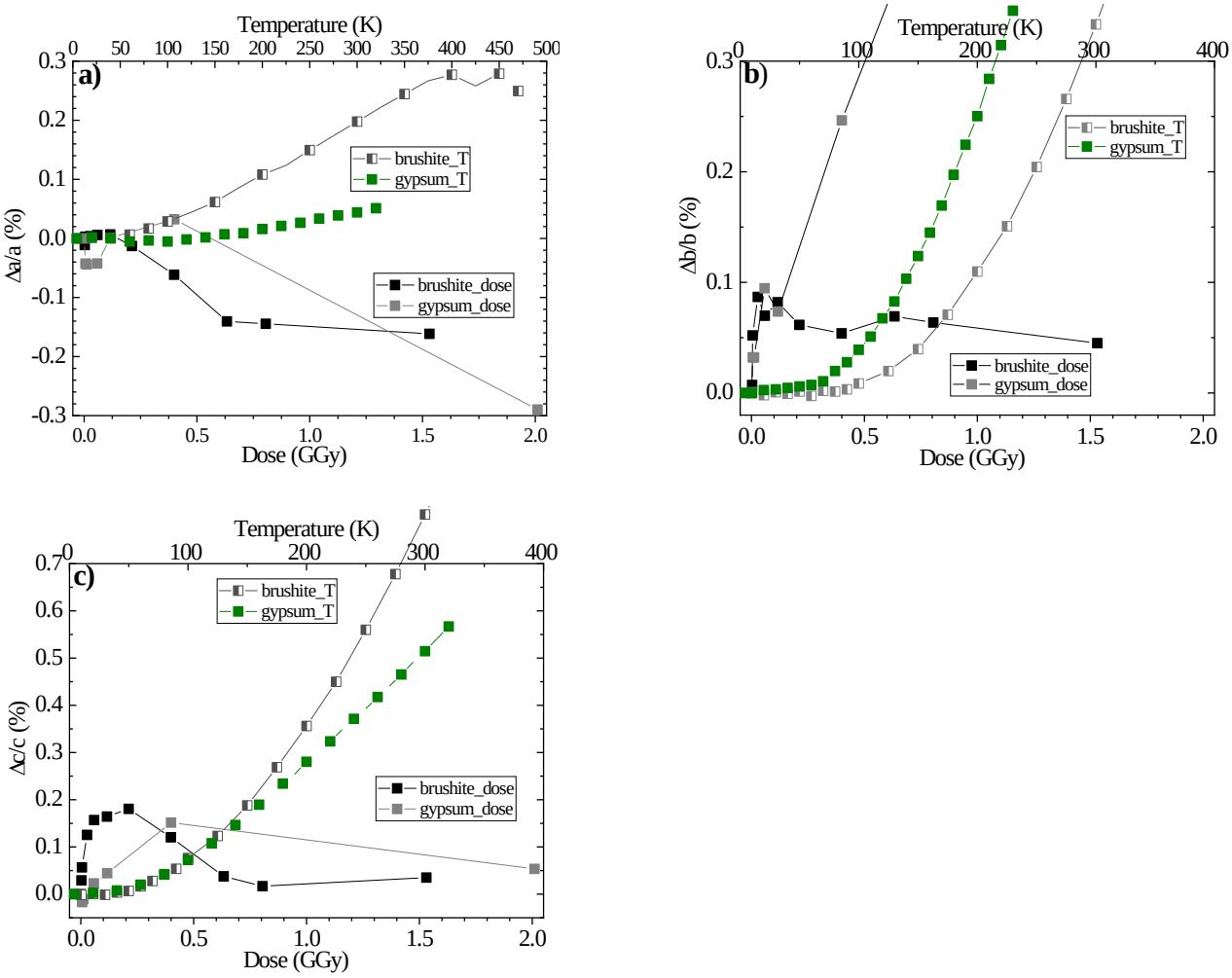


**Fig. 11.** Relative unit cell parameters (Δa/a, Δb/b and Δc/c in %) for brushite and gypsum, versus dose (bottom scale) and temperature (top scale) [34, 46].

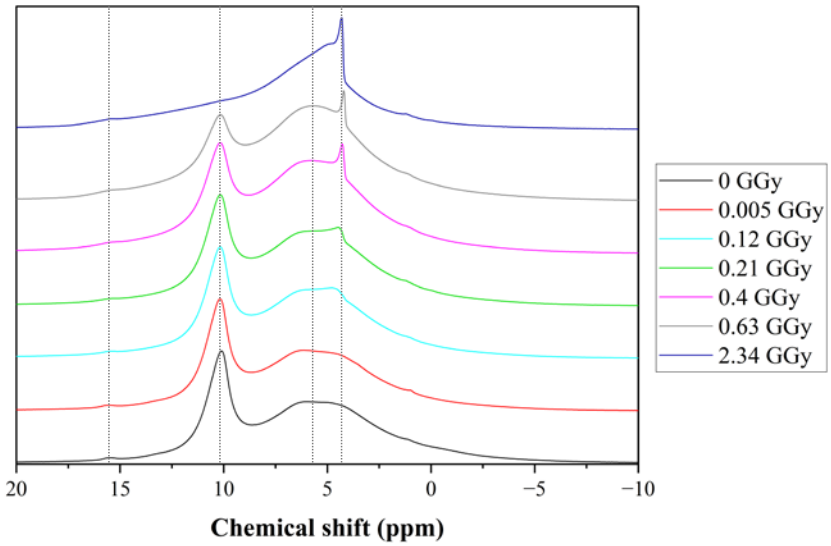


**Fig. 12.** $^{1}$H MAS-NMR spectra of virgin and irradiated brushite samples as a function of the irradiation dose (in GGy). The peak at 10.3 ppm is assigned to the acidic proton (H1 in Fig. 1 – right) [82-84]. The broader peak centered at about 5.5 ppm is attributed to protons in molecular water present in brushite (the isotropic chemical shifts of the four protons in w1 and w2 were calculated at 6.0 (H2 in Fig. 1 – right), 6.9 (H3), 4.6 (H4) and 3.5 ppm (H5) [85, 86] and its degradation product. The centerband of very small intensity at 15.5 ppm is assigned to the hydrogen-bonded acidic protons in monetite [83, 86, 87], present as an impurity (2 wt.%) in the virgin sample. The assignment of the narrow peak at about 4.2 ppm is possibly interpreted as radiolytic $H_2$ gas or as a small amount of partly mobile water.

**Table 1.** Structure, unit cell and atomic parameters (ICSD files) used as starting models used for Rietveld analysis. Atomic models and some structural parameters, and nature of the interlayer interactions for all studied hydrous minerals, after experimental and numeric simulations studies at ambient conditions.
$B_{iso} = 8\pi^2 U_{iso}$ (Å$^2$) thermal factor parameters, resulting from temperature-dependent atomic vibrations

| Mineral | Structure | Unit cell and atomic parameters | Atomic model and some structural parameters | Interlayer bonding | References |
|---|---|---|---|---|---|
| Hydroxide $Ca(OH)_2$ Portlandite | $CdI_2$ –type structure<br>Trigonal layered structure along **c** axis<br>centrosymmetric<br>P-3m1 space group (N°164)<br>Z = 1 | a = 3.5918 Å<br>c = 4.9063 Å<br>V = 54.82 Å$^3$<br>(ICSD N°202220) [31]<br>One-site model<br>Ca: site *1a*<br>O and H: site *2d*<br>(1/3,2/3,z)<br>OH aligned along **c** | Sheets of edge-sharing $CaO_6$ octahedra stacking along **c** axis<br>d(Ca-O) = 2.370 Å [31]<br>Interlayer distances:<br>d(O-O) ~ 3.33 Å, d(H-H) ~ 2.2 Å [31, 42]<br>d(H-H) projected along **c** axis~ 0.73 Å [42]<br>Interlayer distance (projection along **c** axis) = 2.616 Å [42]<br>Unusual thermal motion for H: large and anisotropic [31, 40]<br>Introduction of the three-site split-atom model:<br>H atom: site *6i*(x, 2x, z); OH tilted; $B_{iso}$ (H) = 2.24 Å$^2$ at RT [43] | Weak interlayer forces of type van der Waals<br>No H-bonding | Busing 1957 [40]<br>Chaix 1987 [31]<br>Kruger 1989 [27]<br>Desgranges 1993 [42]<br>Desgranges 1996 [43]<br>Raugei 1999 [52]<br>Xu 2007 [44] |
| Hydroxide $Mg(OH)_2$ Brucite | | a = 3.14979 Å<br>c = 4.7702 Å<br>V = 40.99 Å$^3$<br>(ICSD N°79031) [32]<br>One-site model | Sheets of edge-sharing $MgO_6$ octahedra stacking along **c** axis<br>d(Mg-O) = 2.1003 Å [32],<br>Interlayer distances:<br>d(O-O) = 3.229 Å [32]<br>d(H-H) = 1.984 Å [43], 2.25 Å [53]<br>d(H-H) projected along **c** axis= 0.794 Å [43]<br>Interlayer distance (projection along **c** axis) = 2.689 Å [43]<br>Unusual thermal motion for H: large and anisotropic<br>Three-site split-atom model: $B_{iso}$ (H) = 2.36 Å$^2$ at RT [43] | Weak interlayer forces of type van der Waals<br>very weak interaction between the OH groups<br>No H-bonding | Kruger 1989 [27]<br>d'Arco 1993 [53]<br>Catti 1995 [32]<br>Desgranges 1996 [43]<br>Chakoumakos 1997 [54]<br>Raugei 1999 [52]<br>Xu 2013 [45] |
| $CaSO_4.2H_2O$ Gypsum | Monoclinic layered structure along **b** axis,<br>centrosymmetric<br>C2/c space group (N°15)<br>Z = 4 | *I2/a setting (unique axis **b**)*<br>a = 5.675 Å<br>b = 15.19763 Å<br>c = 6.52291 Å<br>□ = 118.479°<br>V = 494.536 Å$^3$<br>(ICSD N°151692) [33] | Sheets with ziz-zag chains of $CaO_8$ polyedra linked to zig–zag chains of $SO_4^{2-}$ tetrahedra<br>$B_{iso}$ (H1) = $B_{iso}$ (H2) = 6.71 Å$^2$ [33]<br>$B_{iso}$ (D1) = 3.52 Å$^2$; $B_{iso}$ (D2) = 3.07 Å$^2$ [46]<br>One hydrogen bond in the sheets (see Table 2) | Interlayer bonding via water molecules:<br>One type of water molecules (H1-O3-H2)<br>one H bond "along **b** axis"<br>(see Table 2) | Cole 1974 [55]<br>Atoji 1958 [56]<br>Schofield 1996 [46]<br>De la Torre 2004 [33] |
| $CaHPO_4.2H_2O$ Brushite | Monoclinic layered structure along **b** axis,<br>non-centrosymmetric<br>Cc space group (N°9)<br>Z = 4 | Ia *setting (unique axis **b**)*<br>a = 5.8105 Å<br>b = 15.1758 Å<br>c = 6.2337 Å<br>□ = 116.405°<br>V = 492.33 Å$^3$<br>(ICSD N°172258) [34] | Sheets with ziz-zag chains of $CaO_8$ polyedra linked to zig–zag chains of $PO_4^{3-}$ tetrahedra<br>$B_{iso}$ (D1) = 2.13 Å$^2$; $B_{iso}$ (D2) = 1.86 Å$^2$; $B_{iso}$ (D3) = 2.24 Å$^2$;<br>$B_{iso}$ (D4) = 4.14 Å$^2$;$B_{iso}$ (D5) = 4.35 Å$^2$ [34]<br>Two hydrogen bonds in the sheets (see Table 2):<br>one similar to the one in gypsum, the other (via the H1 acidic proton) is absent in gypsum | Interlayer bonding via water molecules:<br>Two types of water molecules w1 (H2-O5-H3) and w2 (H4-O6-H5)<br>two H bonds "along **b** axis"<br>(see Table 2) | Curry 1971 [57]<br>Tortet 1997 [58]<br>Schofield 2004 [34] |

**Table 2**

Interlayer, intralayer and interwater hydrogen bondings in the four compounds of this study. For brushite, hydrogen bond lengths O---H ($d_{O---H)}$ and O---H-O lengths ($d_{O-O}$), according to the structure of Schofield et al. from neutron powder diffraction data at 300K [34] and from IR and neutron scattering data of Tortet et al. [58]. Water oxygens are referred to as O5(**$w_1$**) and O6(**$w_2$**). H-bonding directions are specified when they are rather well aligned with a unit cell axis. For brucite and portlandite, data from the one –site models are reported.

| Compound | H-bonding Intra/Inter-layer | H-bonding along | H bond | $d_{O-O}$ (**O**---H-**O**) (Å) | $d_{O- - -H}$ (Å) | $d_{OH}$ (Å) | Bending angle (°) O---H-O | References |
|---|---|---|---|---|---|---|---|---|
| $CaHPO_4.2H_2O$ Brushite | Intralayer | | **O4**---H1-**O1** (acidic) | 2.676<br>2.68 | 1.705 | H1-O1: 0.988<br>1 | 166.4 | Schofield 2004 [34]<br>Tortet 1997 [58] |
| | | **a** axis | **O3**---H3-**O5**(**$w_1$**) | 2.702<br>2.76 | 1.77 | H3-O5: 0.945<br>0.98 | 166.8 | Schofield 2004 [34]<br>Tortet 1997 [58] |
| | Interlayer | **b** axis | **O3**---H2-**O5**(**$w_1$**) | 2.783<br>2.780 | 1.83 | H2-O5: 0.954<br>0.97 | 172.8 | Schofield 2004 [34]<br>Tortet 1997 [58] |
| | | | **O1**---H4-**O6**(**$w_2$**) | 2.870<br>2.830 | 1.906 | H4-O6: 0.975<br>0.930 | 169.2 | Schofield 2004 [34]<br>Tortet 1997 [58] |
| | Interwater H bond | **c** axis | **O5**(**$w_1$**)---H5-**O6**(**$w_2$**) | 3.073<br>3.090 | 2.171 | H5-O6: 0.925<br>0.900 | 164.6 | Schofield 2004 [34]<br>Tortet 1997 [58] |
| $CaSO_4.2H_2O$ Gypsum | Intralayer | **a** axis | **O1**---H1-**O3**(**w**) | 2.816<br>2.820<br>2.795 | 1.860<br>1.871<br>1.901 | 0.944<br>0.957<br>0.925 | 174.1<br>170.8<br>161.9 | Cole 1974 [55]<br>Schofield 1996 [46]<br>De La Torre 2004 [33] |
| | Interlayer | **b** axis | **O1**---H2-**O3**(**w**) | 2.896<br>2.868<br>2.880 | 1.955<br>1.922<br>1.957 | 0.962<br>0.947<br>0.928 | 172.3<br>177.2<br>173 | Cole 1974 [55]<br>Schofield 1996 [46]<br>De La Torre 2004 [33] |
| $Mg(OH)_2$ Brucite | No H bonding | | | 3.229<br>3.245 | 2.523<br>2.517 | 0.919<br>0.947 | 133.9<br>133.8 | Catti 1995 [32]<br>Desgranges 1996 [43] |
| $Ca(OH)_2$ Portlandite | | | | 3.334<br>3.338 | 2.665<br>2.665 | 0.940<br>0.942 | 128.8<br>128.9 | Chaix 1987 [31]<br>Desgranges 1996 [43] |

**Table 3**

Density ρ, mean excitation energy I, inelastic stopping power and range R estimated using ESTAR [61] for the four studied compounds and 2.5 MeV electrons.

| | Density ($g/cm^3$) | I (eV) | S(E) MeV/cm | R (mm) |
|---|---|---|---|---|
| $Ca(OH)_2$ | 2.24 | 130.7 | 3.73 | 6.3 |
| $Mg(OH)_2$ | 2.39 | 110.6 | 3.99 | 5.9 |
| $CaSO_4.2H_2O$ | 2.32 | 129.7 | 3.83 | 6.2 |
| $CaHPO_4.2H_2O$ | 2.32 | 119.6 | 3.84 | 6.1 |

**Table 4.** Damages produced by 2.5 MeV electron beam to all studied hydrous minerals as a function of experimental conditions.

| Compound (powder) | Dose rate $\phi$ (Gy/s) | I ($\mu$A) | Max T (°C) | Max. dose $\Phi$ (GGy) | Technique | Damages |
|---|---|---|---|---|---|---|
| $Ca(OH)_2$ Portlandite | $1.2 \times 10^4$ | 20<br>25 | 37<T<43<br>42<T<49 | 4 | XRD | Long range order preserved at highest dose. No decomposition into CaO.<br>Unit cell volume and lattice parameters expansion, dependent on calcite content in the sample<br>Anisotropic and asymmetric Bragg line broadening consistent with stacking-fault disorder |
| with various $CaCO_3$ contents (P.1.5, P4, P15) | $1.2 \times 10^4$ | 21-23 | 48<T<50 | 3.1 | IR | |
| $Mg(OH)_2$ Brucite B-PRO | $1.2 \times 10^4$ | 20 | 45<T<50 | 5 | XRD | Long range structural order maintained at highest dose. No decomposition into MgO.<br>Volume expansion: expansion along **c** but slight contraction along **a,** as a function of dose; dependent on the sample (chemistry, microstructure).<br>Anisotropic and asymmetric Bragg line broadening consistent with stacking-fault disorder, more pronounced than in portlandite. |
| B-SA | $1.2 \times 10^4$ | 20 | 40<T<47 | 11.5 | XRD | |
| $CaSO_4.2H_2O$ Gypsum | | 20-25 | 40<T<45 | ~ 1.5 | XRD | For ~ 1.5 GGy, decomposition into crystalline bassanite ($CaSO_4$,1/2 $H_2O$) and anhydrite $CaSO_4$:<br>$CaSO_4,2H_2O \rightarrow CaSO_4,1/2\ H_2O + CaSO_4$ |
| | | 15* | < 36 | ~ 2 | XRD | Progressive decomposition into two crystalline phases:<br>▪ For 6 MGy, only $CaSO_4,2H_2O$, no decomposition.<br>▪ For 60 MGy, partial decomposition into hemi-hydrate $CaSO_4$, $1/2H_2O$<br>▪ For400 MGy, decomposition into hemi-hydrate and a very small amount of anhydrite. |
| $CaHPO_4.2H_2O$ Brushite (**) | $3 \times 10^2$ | 0.5 | 15 | 0.21 | XRD | Amorphization but no decomposition observed at all fluxes, even the lowest.<br>Dose rate dependence of structural damage taking the form of a broadening of the X-ray diffraction lines increasing with decreasing beam current (20 to 5 $\mu$A), suggesting that some annealing of irradiation-induced defects at highest current 20 $\mu$A. |
| | $1 \times 10^3$ | 1.5 | 15 | | | |
| | $3 \times 10^3$ | 5 | 20 | | | |
| | $6 \times 10^3$ | 10 | 30 | | | |
| | $1.2 \times 10^4$ | 20 | 38 | | | |
| | ~$1.1 \times 10^4$ | 18 ± 2 | ≤ 44 | 2.34 | XRD | Amorphization visible for doses as low as 30 MGy.<br>Progressive intensity decrease of all Bragg lines with increasing dose.<br>Broadening of Bragg lines up to 120 MGy.<br>Break in slope of the plot of amorphous fraction vs. dose around 0.7 GGy (Fig. 4b).<br>Amorphization almost complete at ~ 2.34 GGy.<br>$CaHPO_4$ undetectable at any dose, contrary to what happens upon heating. |
| | | | | | Raman | Progressive decrease and broadening of all Raman peaks while others become visible and grow with dose at 351, 739, 1038, 1111 and 1162 $cm^{-1}$, characteristic of the phosphate groups in calcium pyrophosphate [28].<br>Complete transformation into an amorphous pyrophosphate $Ca_2P_2O_7,nH_2O$ attained for doses of ~ few GGy. |
| | | | | | NMR | Acidic H bond would be responsible for full amorphization at highest dose |

* beam current decreased to 15 $\mu$A in order to keep the temperature strictly below 40°C since gypsum starts to loose water at 40°C and forms hemi-hydrate around 70-80°C

** brushite was irradiated also at two lower energies: 1 MeV and 0.5 MeV: amorphization is still observed. No decomposition into monetite $CaHPO_4$.